Title	Modeling and Numerical Analysis of Dislocations and Disclinations Based on Differential Geometry
Author(s)	Sigiet, Haryo Pranoto
Citation	大阪大学, 2024, 博士論文
Version Type	VoR
URL	https://doi.org/10.18910/96106
rights	
Note	

Modeling and Numerical Analysis of Dislocations and Disclinations Based on Differential Geometry

SIGIET HARYO PRANOTO

MARCH 2024

Modeling and Numerical Analysis of Dislocations and Disclinations Based on Differential Geometry

A dissertation submitted to

THE GRADUATE SCHOOL OF ENGINEERING SCIENCE

OSAKA UNIVERSITY

In partial fulfillment of the requirements for the degree of

DOCTOR OF PHILOSHOPY IN ENGINEERING

BY

SIGIET HARYO PRANOTO

MARCH 2024

Abstract

This study aims to employ nonlinear continuum mechanics and differential geometry to model and evaluate dislocation microstructures. The kinematics of the continuum are defined by three configurations: the reference, intermediate, and current configurations, which are formulated on a Riemann-Cartan manifold. The intermediate configuration is determined by solving the Cartan first structure equation, whereas the stress equilibrium equation determines the current configuration. The process of modeling dislocations entails describing them as a continuous dislocation density distribution, and doing numerical analysis through the utilization of the finite element method.

The initial part of the study examines the mechanism of material strengthening by means of kink deformation. At first, we performed a quantitative validation of the current dislocation model by employing grain boundary theory. Afterwards, we simulated the growth mechanism of ortho-type kink deformation by employing an arrangement of edge dislocations. The research indicates a notable concentration of stress near the termination of the kink interface, which is caused by the production of disclinations. The kink-strengthening mechanism is further explained by considering the strain energy, stress field distribution, and elastic interaction between disclinations.

The second issue being examined is to demonstrate the existence of disclinations inside the kink microstructure. Although it is widely accepted that the kinked deformation microstructure contains disclinations, a rigorous mathematical demonstration of this phenomenon is still lacking. This study utilizes the holonomy method to prove the existence of disclinations by the evaluation of the Frank vector. The accuracy of this method is confirmed by employing ortho kink models featuring diverse dislocation arrangements. Subsequently, the ridge kink deformation models utilize the holonomy method to showcase a precise correlation between the holonomy analysis and theoretical predictions. This method offers a numerical assessment of the Frank vector for each given arrangement of dislocations.

Finally, the study examines the effects of size on elasto-plastic deformation in nanoscale materials using the Eshelby twist and twist boundary models. Although the models have different dislocation configurations, they both display the same twisting deformations. The objective is to understand the fundamental mechanism responsible for the twisting deformation in both models by analyzing the distribution of plastic deformation fields. The analysis demonstrates that the Eshelby twist encompasses two plastic deformation components that contribute to the twisting effect, whereas the twist boundary model encompasses four

components. Furthermore, it has been discovered that only Burgers vectors of the same polarity are capable of causing twisting deformation in the twist boundary model. The extent of twisting distortion, known as the twist angle, is especially important at tiny scales.

Table of Contents

List of Figures

Chapter I

General Introduction

1.1. Research background

1.1.1. Lattice defects in nanocrystalline materials

Dislocations are one of the line defects within crystalline solid materials. These defects come in three types: edge dislocations, screw dislocations, and mixed dislocations that contain both types. Their existence in nanocrystalline solids stands as a pivotal lattice defect, exerting influence over the mechanical properties of the materials, encompassing high-yield strength, ductility, and fracture toughness [1].

The Volterra dislocation model stands as one of the most classical representations of dislocations based on continuum mechanics [2]. Within this model, the atomic misalignment resulting from dislocations is represented by discontinuity function that is incorporated into the continuum mechanics analysis. It is widely recognized that this model can accurately reproduce the stress field distant from the dislocation line [1]. Nevertheless, the linear approximation in the constitutive equation falls short in elucidating nonlinear finite deformations, resulting in the emergence of stress singularities within this dislocation model. The issue of stress singularity can be addressed by employing the theory of continuously distributed dislocation density [3]. An early instance of this theory is the Peierls-Nabarro model [4, 5]. This model introduces dislocations distributed continuously in the plane corresponding to the slip surface, with a linear elastic body assumed in the areas both above and below the dislocations. Consequently, each stress component is recognized to be nonsingular [5]. Nevertheless, it is crucial to emphasize that this model does not account for geometrical nonlinearity.

Yavari and Goriely have recently developed a differential geometry-based nonlinear continuum mechanics for dislocations [6]. This is an updated version of the traditional non-Riemannian dislocation theory that was first developed by Kröner and Seeger [9], as well as Kondo [7], Bilby et al [8]. This mathematical framework merges the theories of continuous dislocation distribution and geometrical elasto-plasticity that can simultaneously solve both stress singularities and geometrical nonlinearities. They have also offered analytical solutions under particular boundary conditions for nonlinear stress and strain fields.

1.1.2. Kink deformations and disclinations of the LPSO-type Mg alloys

The Mg alloys exhibiting the long-period stacking ordered (LSPO) type demonstrate excellent mechanical characteristics, characterized by their lightweight nature, high-yield strength, and reasonable plastic elongation [10, 11, 12]. Magnesium predominates in these alloys, with trace amounts of Zn and rare earth metals. Previous research has shown that the unique plastic deformation mode known as kink deformations is responsible for their exceptional mechanical characteristics. These deformations manifest as localized bends within the material and represent a common type of deformation observed in crystalline solids.

Kink band formation in single Cd crystals was first observed by Orowan [13] in the early 1940s [13]. These kink bands commonly form in materials with a layered microstructure, where the active slip direction aligns parallel to the basal plane and undergoes uniaxial compressive loading. It was also pointed out that kink deformation has two distinct morphologies: ortho- and ridge-kinks. Hess and Barret postulated a kink deformation process based on dislocation, derived from the experimental study [14]. They explain how kinks form and grow on the basis of the dislocation motion under compressive loading. Numerous experiments have indicated that the majority of kink bands in LPSO-type Mg alloys originate from kink boundaries characterized by a misorientation angle of less than 15 degrees [1, 15].

Kink deformation has garnered significant interest as a possible novel strengthening mechanism for crystalline materials due to its distinction from the traditional plastic deformation mode. The majority of prior studies have indicated that the strengthening mechanism in kink formation is attributed to dislocations acting as a hindrance to the motion of dislocations. But in this instance, it is important to take into account how disclinations contribute to the kink-strengthening mechanism. Using rank-1 connection analysis, Inamura predicted the presence of disclination at the tip of a ridge-type kink. [16]. It is generally known that crystalline solids that contain isolated disclinations accumulate much higher elastic strain energy than that contain isolated dislocations. To uncover the process of kink strengthening, it will thus be necessary to clarify the existence of disclinations in the LPSO-type Mg alloys.

1.1.3. Eshelby twist and twist boundary in the nanowire materials

With dimensions in the nanometer range, nanomaterials have special mechanical characteristics that set them apart from their bulk counterparts. They are appealing for a variety of applications in fields like electronics, medical, coatings, and other industries because of their special qualities [17]. These nanodevices are closely related to their functions, so it is important to synthesize them while controlling their shape and to assemble the nanomaterials that make up the device in the desired shape. It is known that such nanomaterials may also contain dislocations, and the amount of deformation that occurs in nanomaterials is significantly greater than that in bulk materials. This is the realization of size-dependence of nanomaterials. A typical example of this phenomenon occurs in PbS nanowires due to screw dislocations [18]. A spiral mechanism has been observed for the growth of nanowire materials during deposition, leading to nanowires with screw dislocations at the centre. The morphology of nanowires exhibits a twisted crystal orientation along the longitudinal direction. In addition, this phenomenon has also been observed in other nanowires containing screw dislocations and showed the same results. Furthermore, the finite deformation theory can therefore be used to accurately estimate dislocation-induced deformation in nanomaterials.

1.2. Purpose of the research

This study aims to provide dislocation-based modeling and numerical analysis for lattice defects utilizing nonlinear continuum mechanics based on differential geometry, as described in the previous section. More specifically, we incorporate the dislocation-based model into the planar array of edge dislocations that forms the kink deformation. In addition, nonsingular stress fields, elastic interactions between disclinations, and elastic strain energy are discussed as mechanisms of material strengthening. On the other hand, we also implement the dislocation-based model into Eshelby twist and twist boundary and reveal the similarity between them.

1.3. Structure of this dissertation

This thesis has the following structure. The background of the research and its goals are covered in Chapter 1. The differential geometry theory for dislocations is summarised in Chapter 2. First, we provide the reference $\mathcal{R}$, intermediate $\mathcal{B}$, and current $\mathcal{S}$ states of Riemann-Cartan manifold kinematics. This yields the gradient of plastic deformation, and the Riemannian metric on the intermediate state can be found using this technique. Next, we develop the weak form of the stress equilibrium equation for hyperelastic St. Venant-Kirchhoff material. The gradient of elastic deformation, which is associated with elastic deformation, is provided by this solution. We present the dislocation-based modeling for ortho-kink deformation in chapter 3 and explain how elastic strain energy, the distribution of the stress field, and the interactions between disclinations contribute to kink strengthening. The holonomy analysis to confirm the existence of disclinations by calculating the Frank vector is explained in Chapter 4. Several dislocation configurations for the two-dimensional ridge kink model are built. In chapter 5, screw dislocations are examined and included into the twist boundary and Eshelby twist models. Chapter 6 concludes with some closing remarks.

Chapter II

Modeling of Lattice Defects Based on Continuum Mechanics and Differential Geometry

2.1. Linear and nonlinear elasticity theories

2.1.1. Linear elasticity theory

We begin by partitioning the smooth boundary $\partial\Omega$ of a three-dimensional elastic body Ω into two distinct subsets: Γ_D and Γ_N. Here, Γ_D represents a Dirichlet boundary condition exhibiting zero displacements, while Γ_N denotes a Neumann boundary condition involving surface tractions. The entire region of Ω is subject to both a volume force f_i (where $i = 1, \ldots, n$) and a surface force g_i acting on Γ_N. Let u_i represents the displacement of Ω resulting from external forces. For the displacement vector $u_i(x)$ within an n-dimensional elastic body, the strain tensor ϵ_{ij} is defined as follows

$$\epsilon_{ij} = \frac{1}{2}\left(\frac{\partial u_i}{\partial x_j} + \frac{\partial u_j}{\partial x_i}\right) \tag{2. 1}$$

The elastic constant tensor of an isotropic elastic body is defined using Lamé constants λ and μ as follows.

$$C_{ijkl} = \lambda\delta_{ij}\delta_{kl} + \mu\delta_{ik}\delta_{jl} + \mu\delta_{il}\delta_{jk} \tag{2. 2}$$

Moreover, the stress tensor σ_{ij} of an n-dimensional elastic body is defined from Hooke's law using the elastic constant tensor C_{ijkl} as

$$\sigma_{ij} = C_{ijkl}\epsilon_{kl} \tag{2. 3}$$

The connection between σ_{ij} and ϵ_{ij}, which defines the stress-strain relationship, is called the constitutive equation. Additionally, the strain energy density W of an n-dimensional elastic body is defined as

$$W = \frac{1}{2}C_{ijkl}\epsilon_{ij}\epsilon_{kl} = \frac{1}{2}\sigma_{ij}\epsilon_{ij} \tag{2. 4}$$

Therefore, the functional $I[u_i]$ is thus defined as

$$I[u_i] = \int_{\Omega} W dV - \int_{\Omega} f_i u_i dV - \int_{\Omega} g u_i dS \tag{2. 5}$$

Following the variational principle, the functional $I[u_i]$ becomes a stationary value when its first variant δI equals zero. Let α be a small quantity $(|\alpha| \ll 1)$, and h_i be any function that is continuously differentiable, satisfying zero at Γ_D. Consider the transformation $u_i \rightarrow u_i + \alpha h_i$, the resulting change in the functionals is denoted as $\Delta I = I[u_i + \alpha h_i] - I[u_i]$. Here, $\Delta I = \alpha \delta I + O(\alpha^2)$, where the primary linear term δI represents the first variation of the functional I. Based on the definition we have,

$$\begin{aligned} \Delta I = \int_{\Omega} \left(W\left(u_{i,j} + \alpha h_{i,j}\right) - f_i(u_i + \alpha h_i) \right) dV \\ - \int_{\Gamma_N} g_i(u_i + \alpha h_i) dS - \int_{\Omega} \left(W\left(u_{i,j}\right) - f_i u_i\right) dV + \int_{\Gamma_N} g_i u_i dS \qquad (2. 6) \\ = \int_{\Omega} \left(W\left(u_{i,j} + \alpha h_{i,j}\right) - W\left(u_{i,j}\right) \right) dV - \alpha \int_{\Omega} f_i h_i dV - \alpha \int_{\Gamma_N} g_i h_i dS\,. \end{aligned}$$

The first term on the right side of the equation's Taylor expansion yields

$$\int_{\Omega} \left(W\left(u_{i,j} + \alpha h_{i,j}\right) - W\left(u_{i,j}\right) - W\left(u_{i,j}\right) \right) dV = \alpha \int_{\Omega} \frac{\partial W}{\partial u_{i,j}} h_{i,j} dV + O(\alpha^2). \tag{2. 7}$$

As a result, the first variation δI of the functional becomes

$$\begin{aligned} \delta I = \left. \frac{dI[u_i + \alpha h_i]}{d\alpha} \right|_{\alpha=0} &= \int_{\Omega} \frac{\partial W}{\partial u_{i,j}} h_{i,j} dV - \int_{\Omega} f_i h_i dV \int_{\Gamma_N} g_i h_i dS \\ &= \int_{\Omega} C_{ijkl} \epsilon_{kl} h_{i,j} dV - \int_{\Omega} f_i h_i dV - \int_{\Gamma_N} g_i h_i dS. \end{aligned} \tag{2. 8}$$

Therefore, based on the variational principle where δI equals zero, we obtain

$$\int_{\Omega} C_{ijkl} \epsilon_{kl} h_{i,j} dV - \int_{\Omega} f_i h_i dV - \int_{\Gamma_N} g_i h_i dS = 0. \tag{2. 9}$$

In this case, the variational principle applied to the functional I yielded an equation known as the equation of stress equilibrium in its weak form.

2.1.2. Nonlinear elasticity theory

It is widely recognized that linear elasticity is only applicable for infinitesimal deformation, *i.e.*, it cannot be used for large plastic deformation. As indicated in Equation (2. 1), it is called Cauchy strain, which remains solely accurate for small deformations. Therefore, for large deformations, the following equation can be employed

$$E_{ij}(u_i) = \frac{1}{2}\left(\frac{\partial u_i}{\partial X_j} + \frac{\partial u_j}{\partial X_i} + \frac{\partial u_m}{\partial X_i}\frac{\partial u_m}{\partial X_j}\right). \tag{2. 10}$$

This is referred to as the Green strain tensor. Equation (2. 10) above illustrates the Green strain tensor includes a squared term related to the displacement u_i, specifically the second term on the right-hand side. This term is recognized as the geometric nonlinearity term. In the following, the equilibrium equation of weak form stress in nonlinear elasticity theory is derived using the variational principle as is the case of linear elasticity theory.

$$\begin{aligned} E_{ij}\left(u_{i,j} + \alpha h_{i,j}\right) &= E_{ij}\left(u_{i,j}\right) + \frac{1}{2}\left(\frac{\partial h_i}{\partial X_j} + \frac{\partial h_j}{\partial X_i} + \frac{\partial h_m}{\partial X_i}\frac{\partial u_m}{\partial X_j} + \frac{\partial u_m}{\partial X_i}\frac{\partial h_m}{\partial X_j}\right) + O(\alpha^2) \\ &= E_{ij}\left(u_{i,j}\right) + \alpha dE_{ij}\left(u_{i,j}, h_{i,j}\right) + O(\alpha^2) \end{aligned} \tag{2. 11}$$

Thus, we obtain

$$dE_{ij}\left(u_{i,j}, h_{i,j}\right) = \frac{1}{2}\left(\frac{\partial h_i}{\partial X_j} + \frac{\partial h_j}{\partial X_i} + \frac{\partial h_m}{\partial X_i}\frac{\partial u_m}{\partial X_j} + \frac{\partial u_m}{\partial X_i}\frac{\partial h_m}{\partial X_j}\right) \tag{2. 12}$$

Next, concerning the strain energy density in Equation (2. 4), we also consider the transformation of displacement $u_{i,j} \to u_{i,j} + \alpha h_{i,j}$ such that

$$\begin{aligned} W = \left(u_{i,j} + \alpha h_{i,j}\right) &= \frac{1}{2} C_{ijkl} E_{ij}\left(u_{i,j} + \alpha h_{i,j}\right) E_{kl}\left(u_{i,j} + \alpha h_{i,j}\right) \\ &= W\left(u_{i,j}\right) + \alpha C_{ijkl} dE_{ij}\left(u_{i,j}, h_{i,j}\right) E_{kl}\left(u_{i,j}\right) + O(\alpha^2) \end{aligned} \tag{2. 13}$$

The equilibrium equation for the weak form stress in nonlinear elasticity theory is derived from the variational principle, and it is as follows

$$\int_{\Omega} C_{ijkl} dE_{ij}\,(u_i, h_i) E_{kl}(u_i) dV = \int_{\Omega} f_m h_m dV + \int_{\Gamma_N} g_m h_m dS. \tag{2. 14}$$

2.2. Dislocation mechanics based on differential geometry

This section provides definitions of Riemannian metrics and affine connections, which generalize inner products and directional derivatives from Euclidean spaces to manifolds. These features play a crucial role in the theory of geometric lattice defects. The Riemannian metric and connection serve to generalize the inner product and vector translation from Euclidean space to other spaces, such as manifolds. Connections are characterized by their torsion tensor and curvature tensor, and lattice defect modeling is carried out in connection, without affecting the Riemann metric. This implies that a single Riemannian metric can define two manifolds with different connections.

2.2.1. Riemannian Metrics

The set of tangent vectors at point x on the manifold M creates a vector space referred to as the tangent space T_xM. Within this tangent space T_xM, the equation defines a symmetric bilinear map that is non-negative given by the following equation

$$g_x : T_xM \times T_xM \to \mathbb{R}, \quad x \in M. \tag{2. 15}$$

By definition, this map constitutes the inner product within the tangent space T_xM. When this inner product is assigned to all points across the manifold, and denoted by C^∞ as the collection of inner products $g = \{g_x\}_{x\in M}$, it is termed a Riemannian metric. This g serves as a Riemannian metric for any C^∞ class vector field on the manifold M, where $g(X, Y)$ is a C^∞ function on manifold. A manifold M having a Riemannian metric g attached to it is called a Riemannian manifold. In local coordinates, g_x is expressed in terms of the local coordinate system z as follows

$$g_x = g_{ij}(x)\left(dz^i\right) \otimes \left(dz^j\right). \tag{2. 16}$$

The magnitude of the tangent vector X_x at a specific point x on the manifold can be determined using the Riemannian metric $g(x)$ established on the manifold M. This is achieved through the evaluation of the inner product of the tangent vector X_x, as indicated by the following expression

$$|X_x| = \sqrt{g_x(X_x, Y_x)}. \tag{2. 17}$$

Within Riemannian geometry, the notion of the angle between two tangent vectors X_x and Y_x at a point x on the manifold M holds significant relevance in understanding the geometry of the manifold. The angle created by the inner product g_x between the vectors in the tangent space T_xM is the exact definition of this angle. To be more precise, the angle θ between X_x and Y_x is determined by the following equation

$$\theta(X_x, Y_x) = \cos^{-1}\left(\frac{g_x(X_x, Y_x)}{|X_x||Y_x|}\right), \tag{2. 18}$$

where $|X_x|$ and $|Y_x|$ represent the magnitudes of the tangent vectors X_x and Y_x, respectively.

2.2.2. Affine connection

An affine connection represents a framework that specifies the directional derivative on a manifold *M*. Consider $\bar{X}(M)$ as the collection of all C^∞ class vector fields within the manifold *M*, and let $\forall X \in \bar{X}(M)$ denote any C^∞ class vector field on *M*. A mapping $\nabla: \bar{X}(M) \times \bar{X}(M) \to \bar{X}(M)$ is termed an affine connection on *M* if it adheres to the following property:

- The first parameter should exhibit $C^\infty(M)$ linearity: $\nabla(f(X) + hY, ZX) = f\nabla(X, Z) + h\nabla(Y, Z), \forall X, Y, Z \in \bar{X}(M), \forall f, h \in C^\infty(M)$.
- Fulfills the Leibnitz rule with respect to the second parameter: $\nabla(X, fY) = X[f]Y + f\nabla(X, Y), X, Y \in \bar{X}, a \in \mathbb{R}$.

In this case, the directional derivative of the function f with respect to the vector field X is represented by $X[f]$, this can be expressed in local coordinates as:

$$X[f] = X^i \frac{\partial}{\partial z^i} \tag{2. 19}$$

Likewise, the local coordinate representation for the directional derivative of vector X with respect to Y can be derived using the definition of affine connection ∇ in the following manner

$$\nabla_X Y = \left(X^i \frac{\partial Y^k}{\partial z^i} + \Gamma_{ij}^k X^i Y^j\right)\frac{\partial}{\partial z^k}. \tag{2. 20}$$

Here, Γ_{ij}^k represents the connection coefficient, and the method for directional differentiation is determined based on the connection coefficient Γ_{ij}^k. Moreover, it is possible to construct an infinite number of affine connections ∇ that satisfy the two given properties on a manifold *M*. These distinct affine connections can be differentitated by examining the geometric characteristics attributed to ∇, the torsion tensor T, and the curvature tensor R. The definitions for each of these connections are provided below

$$T(X,Y) = \nabla_X Y - \nabla_Y X - [X,Y], \tag{2. 21}$$

$$R(X,Y)Z = \nabla_X \nabla_Y Z - \nabla_Y \nabla_{\mathrm{X}} Z - \nabla_{[X,Y]} Z. \tag{2. 22}$$

The expression $[X,Y]$ refers to the Lie bracket product of the vector fields X and Y. This product can also be represented in local coordinates as follows

$$[X,Y] = \left(X^i \frac{\partial Y^j}{\partial z^i} - Y^i \frac{\partial X^j}{\partial z^i} \right) \frac{\partial}{\partial z^j} \tag{2. 23}$$

In a manifold *M* equipped with a Riemannian metric g, an affine connection ∇ is considered compatible with the metric g when it meets a specific condition.

$$Z_g(Z,Y) = g(\nabla_z X, Y) + g(Z, \nabla_Z Y) \tag{2. 24}$$

2.2.3. Weitzenböck connection

The Weitzenböck connection, which exhibits a non-zero torsion tensor and a zero-curvature tensor, aligns with the Riemannian metric g. The connection coefficient Γ_{ij}^k can be employed to describe each coefficient of the torsion tensor T_{jk}^i associated with the Weitzenböck connection in the subsequent way

$$T_{jk}^i = \Gamma_{jk}^i - \Gamma_{kj}^i \tag{2. 25}$$

In other words, the connection coefficients Γ_{jk}^i for the Weitzenböck connection exhibit asymmetric when the subscripts interchanged, aligning with the coefficients T_{jk}^i of the torsion tensor. An affine connection with a non-zero curvature tensor and a non-zero torsion, the Levi-Civita connection is found to be in line with the Riemann metric g. Thus, the connection coefficient Γ_{jk}^i is represented as

$$\Gamma_{jk}^i = \frac{g^{il}}{2} \left(\frac{\partial g_{lj}}{\partial z^k} + \frac{\partial g_{lk}}{\partial z^j} - \frac{\partial g_{jk}}{\partial z^l} \right) \tag{2. 26}$$

Here, g^{il} represents each component of the inverse matrix formed when g_{ij} is considered as a matrix, specifically the inverse matrix corresponding to the Riemannian metric g_{ij}. Therefore, using these connection coefficients allows the expression of the curvature tensor for the Levi-Civita connection as follows

$$R_{jkl}^i = -\frac{\partial \Gamma_{kj}^i}{\partial z^l} + \frac{\partial \Gamma_{lj}^i}{\partial z^k} - \Gamma_{lm}^i \Gamma_{kj}^m + \Gamma_{km}^i \Gamma_{li}^m \tag{2. 27}$$

The curvature tensor associated with the Levi-Civita connection is sometimes referred to as the Riemann curvature tensor.

2.2.4. Kinematics of Riemann-Cartan manifold

The geometric lattice defect theory in Riemann-Cartan manifolds outlines the kinematics of a continuum containing lattice defects. The reference, intermediate, and current states are the three states that are used in this framework to express the kinematics of the continuum, as shown in

Figure 2. 1. The reference state signifies a perfect crystal, the intermediate state represents a virtual state accomodating lattice mismatch due to defects, and the current state corresponds to a mechanical equilibrium state that incorporates elastic relaxation caused by lattice mismatch. The deformation gradient can be deecomposed multiplicatively as $F = F_e \cdot F_p$, is linked to these states. The deformation gradients are represented by the symbols F_p and F_e, respectively.

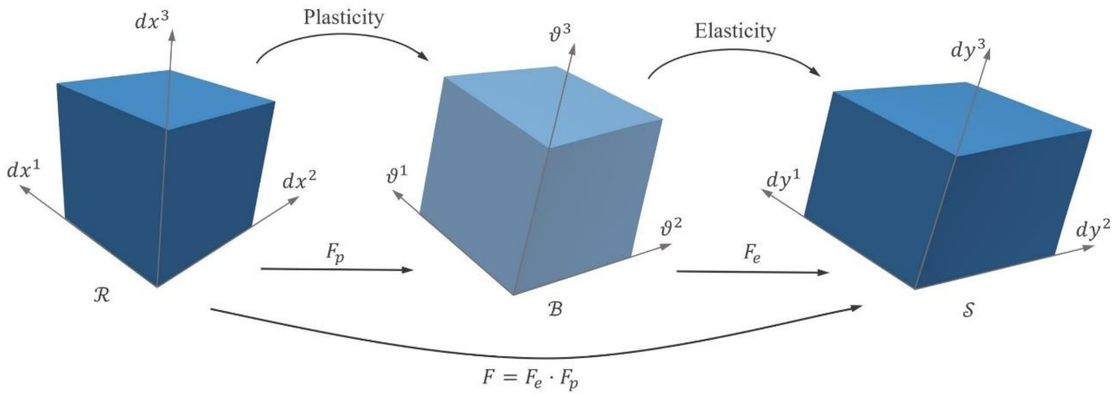

Figure 2. 1 demonstrates that elasto-plastic deformation can be determined as the product of elastic deformation F_e and the plastic deformation F_p, as expressed as $F = F_e \cdot F_p$.

The line elements representing the three states are noted as $(dx^i) = (dx^1, dx^2, dx^3)$, $(\vartheta^i) = (\vartheta^1, \vartheta^2, \vartheta^3)$, and $(dy^i) = (dy^1, dy^2, dy^3)$, respectively. Consequently, the linear transformations are defined by the deformation gradients, leading to:

$$\vartheta^i = \left(F_p\right)^i_j dx^j, \quad dy^i = (F_e)^i_j \vartheta^j, \quad dy^i = F^i_j dx^j = (F_e)^i_k \left(F_p\right)^k_j dx^j. \tag{2. 28}$$

The right Cauchy-Green tensors of each state can represented by the Riemann metrics $g_{\mathcal{R}}, g_{\mathcal{B}}$, and $g_{\mathcal{S}}$. The Riemann metric associated with each state can be expressed in the following forms

$$g_{\mathcal{R}} = \delta_{ij} dx^i \otimes dx^j \tag{2. 29}$$

$$g_{\mathcal{B}} = \delta_{ij} \vartheta^i \otimes \vartheta^j = \delta_{ij} \left(F_p\right)^i_k \left(F_p\right)^j_l dx^k \otimes dx^l \tag{2. 30}$$

$$g_{\mathcal{S}} = \delta_{ij} dy^i \otimes dy^j = \delta_{ij} (F_e)^i_k (F_e)^j_l \vartheta^k \otimes \vartheta^l = \delta_{ij} \frac{\partial y^i}{\partial x^k} \frac{\partial y^j}{\partial x^l} dx^k \otimes dx^l \tag{2. 31}$$

Furthermore, the Green strain tensor E quantifies the elastic deformation by measuring the disparity between the Riemannian metric in the present state and the intermediate state.

$$E = \frac{1}{2}(g_{\mathcal{S}} - g_{\mathcal{B}}) = \frac{\delta_{ij}}{2}\left((F_e)^i_k (F_e)^j_l - \left(F_p\right)^i_k \left(F_p\right)^j_l\right) dx^k \otimes dx^l. \tag{2. 32}$$

This equation quantifies the elastic strain discrepancy between the current and intermediate states, revealing the effect of lattice defects inducing lattice mismatches.

2.3. Cartan first structure equation

We demonstrate how to solve the Cartan first structure equation for a given distribution of dislocations in order to determine the intermediate state $\mathcal{B}$. It is known that in a Weitzenböck manifold, the torsion tensor T^i_{jk} satisfies the Cartan first structure equation as follows

$$T^i_{jk} - \left(\frac{\partial \left(F_p\right)^i_k}{\partial x^j} - \frac{\partial \left(F_p\right)^i_j}{\partial x^k} \right) = 0. \tag{2. 33}$$

Here, T^i_{jk} represents the torsion tensor, and $\left(F_p\right)^i_j$ denotes the plastic deformation gradient. Equation (2. 32) involves $\left(F_p\right)^i_j$, which is obtained by solving the subsequent optimization problem related to the provided torsion tensor T^i_{jk}.

$$\text{Minimize } \mathcal{G}\left[F_p\right] + \mathcal{L}\left[F_p, \lambda\right], \tag{2. 34}$$

$$\text{Subject to } \left(F_p\right)^i_j N^j = 0. \tag{2. 35}$$

The function $\mathcal{G}\left[F_p\right]$ signifies the residual norm within the Cartan first structure equation associated with F_p. Meanwhile, $\mathcal{L}\left[F_p, \lambda\right]$ represents a functional involving F_p and an unspecified multiplier λ, derived through the Lagrange undetermined multiplier method. Furthermore, N denotes the normal vector field at the boundary of the reference state that yields the unit normal vector. The expressions for $\mathcal{G}$ and $\mathcal{L}$ are outlined as follows

$$\mathcal{G} = \frac{1}{2}\int_{\mathcal{R}} \sum_{j<k} \delta_{il} c^i_{jk} c^l_{jk} dV \tag{2. 36}$$

$$\mathcal{L} = \int_{\mathcal{R}} \left(-\delta_{il}\lambda^l \delta_{jk} \frac{\partial \left(F_p\right)^i_j}{\partial x^k} \right) dV \tag{2. 37}$$

Here, c^i_{jk} is represented as

$$c^i_{jk} = T^i_{jk} - \left(\frac{\partial \left(F_p\right)^i_k}{\partial x^j} - \frac{\partial \left(F_p\right)^i_j}{\partial x^k} \right). \tag{2. 38}$$

The variables F_p and λ are determined using the variational principle for the optimization problem in Equations (2. 34) and (2. 35) concerning the Cartan first structure equation. Consider H as a test function satisfying $H^i_j N^j = 0$, and ϵ as a positive real number. By substituting $\left(F_p\right)^i_j$ in Equation (2. 38) with $\left(F_p\right)^i_j + \epsilon H^i_j$ to obtain $c^i_{jk}(\epsilon)$, the first variation $\delta\mathcal{G}\left[F_p\right]$ of $\mathcal{G}\left[F_p\right]$ can be expressed as follows

$$\begin{aligned}
\delta\mathcal{G}\left[F_p\right] &= \left.\frac{d}{d\epsilon}\right|_{\epsilon=0} \frac{1}{2}\int_{\mathcal{R}} \sum_{j<k} \delta_{il} c^i_{jk}(\epsilon) c^l_{jk}(\epsilon) dV \\
&= \int_{\mathcal{R}} \sum_{j<k} \delta_{il} \frac{dc^i_{jk}(\epsilon)}{d\epsilon} c^l_{jk}(\epsilon) dV \\
&= \int_{\mathcal{R}} \sum_{j<k} \delta_{il} \cdot \frac{d}{d\epsilon} \left(T^i_{jk} - \left(\frac{\partial}{\partial x^j} \left(\left(F_p\right)^i_k + \epsilon H^i_k \right) - \frac{\partial}{\partial x^k} \left(\left(F_p\right)^i_j + \epsilon H^i_j \right) \right) \cdot c^l_{jk}(\epsilon) dV \right) \\
&= \int_{\mathcal{R}} \sum_{j<k} \delta_{il} \cdot \left(\frac{\partial H^i_k}{\partial x^j} - \frac{\partial H^i_j}{\partial x^k} \right) \cdot c^l_{jk}(\epsilon) dV \\
&= \int_{\mathcal{R}} \sum_{j<k} \delta_{il} \left(\frac{\partial H^i_k}{\partial x^j} - \frac{\partial H^i_j}{\partial x^k} \right) \left(\frac{\partial \left(F_p\right)^l_k}{\partial x^j} - \frac{\partial \left(F_p\right)^l_j}{\partial x^k} \right) dV
\end{aligned} \tag{2. 39}$$

On the other hand, the first variant $\delta\mathcal{L}\left[F_p, \lambda\right]$ of $\mathcal{L}\left[F_p, \lambda\right]$ is expressed by substituting $\left(F_p\right)^i_j$ in Equation (2. 37) with $\left(F_p\right)^i_j + \epsilon H^i_j$, and replacing λ by $\lambda + \epsilon\eta$ as a test function as follows

$$
\begin{aligned}
\delta\mathcal{L}[F_p,\lambda] &= \frac{d}{d\epsilon}\bigg|_{\epsilon=0}\int_{\mathcal{R}}\left(-\delta_{il}(\lambda^l+\epsilon\eta^l)\delta_{jk}\frac{\partial}{\partial x^k}\left(\left(F_p\right)^i_j+\epsilon H^i_j\right)\right)dV \\
&= \int_{\mathcal{R}}\left(-\delta_{il}\eta^l\delta_{jk}\frac{\partial}{\partial x^k}\left(\left(F_p\right)^i_j+\epsilon H^i_j\right)-\delta_{il}(\lambda^l+\epsilon\eta^l)\delta_{jk}\frac{\partial}{\partial x^k}H^i_j\right)dV \\
&= \int_{\mathcal{R}}\left(-\delta_{il}\eta^l\delta_{jk}\frac{\partial\left(F_p\right)^i_j}{\partial x^k}-\delta_{il}\lambda^l\delta_{jk}\frac{\partial H^i_j}{\partial x^k}\right)dV \\
&= \int_{\mathcal{R}}\left(-\delta_{il}\eta^l\delta_{jk}\frac{\partial\left(F_p\right)^i_j}{\partial x^k}\right)dV+\int_{\mathcal{R}}\left(-\delta_{il}\lambda^l\delta_{jk}\frac{\partial H^i_j}{\partial x^k}\right)dV
\end{aligned}
\tag{2. 40}
$$

The integral parts in the first and second terms of Equation (2. 40) adhere to the subsequent relation:

$$
\begin{aligned}
\delta\mathcal{L}[F_p,\lambda] = &\int_{\partial\mathcal{R}}\left(-N^k\cdot\left(\delta_{il}\eta^l\delta_{jk}\left(F_p\right)^i_j\right)\right)s_{\mathcal{R}}+\int_{\mathcal{R}}\delta_{il}\frac{\partial\eta^l}{\partial x^k}\delta_{jk}\left(F_p\right)^i_j dV \\
&+\int_{\partial\mathcal{R}}\left(-N^k\cdot\left(\delta_{il}\lambda^l\delta_{jk}H^i_j\right)\right)s_{\mathcal{R}}+\int_{\mathcal{R}}\delta_{il}\frac{\partial\lambda^l}{\partial x^k}\delta_{jk}H^i_j dV
\end{aligned}
\tag{2. 41}
$$

Additionally, the conditionals for $\left(F_p\right)^i_j$ and H^i_j are

$$
\begin{aligned}
\left(F_p\right)^i_j N^j &= 0 \\
H^i_j N^j &= 0
\end{aligned}
\tag{2. 42}
$$

Consequently, the expression (2. 41) can be reformulated as follows

$$
\delta\mathcal{L}[F_p,\lambda] = \int_{\mathcal{R}}\left(\delta_{ij}\frac{\partial\eta^l}{\partial x^k}\delta_{jk}\left(F_p\right)^i_j+\delta_{il}\frac{\partial\lambda^l}{\partial x^k}\delta_{jk}H^i_j\right)dV. \tag{2. 43}
$$

In order to stabilize the numerical computations and resolve the ambiguity associated with λ and η, Equation (2. 43) is redefined by introducing new undefined multipliers r and s, presented as follows

$$
\delta\mathcal{L}[F_p,\lambda] = \int_{\mathcal{R}}\left(\delta_{ij}\frac{\partial\eta^l}{\partial x^k}\delta_{jk}\left(F_p\right)^i_j+\delta_{il}\frac{\partial\lambda^l}{\partial x^k}\delta_{jk}H^i_j\right)dV. \tag{2. 44}
$$

By solving the weak form $\delta\mathcal{G}+\delta\mathcal{L}=0$ through the variational principle, F_p and λ can be derived for any arbitrary dislocation distribution T^i_{jk}. This approach allows the determination of the Riemann metric g for the intermediate state $\mathcal{B}$, as explained in the preceding section. To solve this weak form and find F_p and g for different dislocation configurations.

Chapter III

Differential Geometry-Based Nonlinear Continuum Mechanics Modeling and Numerical Analysis of Kink Deformation

3.1. Introduction

Magnesium alloys possessing the long-period stacking ordered (LPSO) structure demonstrate remarkable mechanical properties, including a lightweight composition, a yield strength above 600 Mpa, and a satisfactory plastic elongation [10, 11, 12]. These alloys are mostly made of magnesium, with trace amounts of zinc and rare earth metals. These constituents organize into clusters that align along the basal plane of the hexagonal lattice, producing a layered microstructure with the α-Mg and LPSO phases arranged in sequential order. This unique microstructural feature is commonly known as the mille-feuille structure. Previous research has revealed that kink deformation, a special kind of plastic deformation, is the source of the improved mechanical characteristics of LPSO-Mg alloys. Consequently, kink deformation has garnered considerable attention as a potential novel mechanism for enhancing the strength of crystalline solids.

Orowan first proposed the idea of kink deformation in the 1940s after making an important discovery while performing uniaxial compression on a single cadmium (Cd) crystal [13]. This study notably looked at circumstances in which kink deformation developed when the loading direction was parallel to the basal plane. Further studies employing Zn single crystals conducted by other researchers verified the existence of kink bands [19, 20]. These investigations revealed that kink deformation is common in multilayer structures when the direction of active slip is restricted within a plane parallel to the compression direction. Furthermore, a dislocation-based kink deformation model was put forth in light of Hess and Barret experimental studies. By taking into account the avalanche of edge dislocations, this model explains the nucleation, growth, and feature of severe bending deformation close to the kink interface. It is presently unclear how to quantitatively validate this concept, despite the fact that it offers a phenomenological knowledge of the macroscopic morphology and kink microstructure.

Studies conducted by Tokuzumi and Inamura have revealed a strong correlation between the generation of disclinations and kink deformation, based on both theoretical and experimental evidence [21, 16]. However, the precise way in which the mechanisms of kink deformation and disclinations contribute to strengthening the material remains unclear. One reason for the difficulty in understanding kink deformation is the challenge of using continuum mechanics to model dislocations. Since the constitutive equation uses a linear approximation, classical dislocation theory is unable to adequately explain stress fields surrounding the dislocation core and nonlinear finite deformation [2, 1]. As a result, it is inappropriate for kink deformation analysis. Subsequently, assuming a continuous distribution of dislocation density and providing analytical solutions for nonlinear stress fields, Yavari and Goriely [6] have made significant progress in developing a nonlinear continuum mechanics approach for dislocations on the basis of differential geometry, which was first proposed by Kondo [7], Bilby *et al*. [8], and Kröner *et al.* [9]. This theory, however, has drawbacks when it comes to kink deformation analysis because it necessitates a high number of dislocations. In order to tackle these challenges, Kobayashi and Tarumi [3] proposed a weak-form formulation of the geometrical dislocation theory into finite element analysis. A dislocation-based model for kink deformation that incorporates geometrical nonlinearity without leading to stress singularity can be constructed by applying this theoretical framework.

This work aims to develop a kink deformation model based on dislocation using differential geometry-based nonlinear continuum mechanics. Furthermore, we seek to analyse the stress fields around a kink interface and find out how the kink deformation affects the strength of LPSO-Mg alloys. Here, we provide a quick overview of the study. An outline of the differential geometry based theory for dislocations is given in the next section. First, we present the Riemann-Cartan manifold kinematics, which comprises three different states. More specifically, taking into account the specified dislocation distribution, the intermediate state is found using the Cartan first structure equation. The stress equilibrium equation for St. Venant-Kirchhoff hyperelastic material is then derived in weak form. We solve these two governing equations using the finite element method in order to do the numerical analysis. We next go on to show the outcomes of the numerical analysis. First, we check that our model is accurate by looking at the bending angle that the deformation field causes. Next, in order to comprehend the kink growth process, we examine the elastic strain energy involved and examine the accompanying stress fields. Finally, we examine how the elastic interaction of disclinations and self-energy lead to material strengthening mechanisms.

3.2.Mechanics of Dislocations Using Differential Geometry

3.2.1. Kinematics of Riemann-Cartan manifold

The explanation of dislocation kinematics is elucidated within the framework of the Riemann-Cartan manifold. This framework pertains to a preexisting mathematical framework

[6, 3]. This mathematical framework consists of three different states of a continuum: the initial state $\mathcal{R}$, the intermediate state $\mathcal{B}$, and the final state $\mathcal{S}$. Moreover, these configurations are also associated with the multiplication of the deformation gradients, expressed as $F = F_e \cdot F_p$.

Let's have a look at the local coordinate systems $(dx^i) = (dx^1, dx^2, dx^3)$, $(\vartheta^i) = (\vartheta^1, \vartheta^2, \vartheta^3)$, and $(dy^i) = (dy^1, dy^2, dy^3)$ that are defined on the three states. Deformation gradients play a vital role in establishing the linear transformations that

$$\vartheta^i = \left(F_p\right)^i_j dx^j, \quad dy^i = (F_e)^i_j \vartheta^j, \quad dy^i = F^i_j dx^j = (F_e)^i_k \left(F_p\right)^k_j dx^j. \tag{3. 1}$$

Likewise, the right Cauchy-Green tensors can be defined using the deformation gradient in the following manner.

$$\begin{gathered} I = \delta_{ij}\, dx^i \otimes dx^j, \qquad C_p = \delta_{ij} \left(F_p\right)^i_k \left(F_p\right)^j_l dx^k \otimes dx^l, \\ C = \delta_{ij}\, (F)^i_k (F)^j_l dx^k \otimes dx^l. \end{gathered} \tag{3. 2}$$

Here, the symbol δ_{ij} represents the Kronecker delta, which is a mathematical notation indicating the equality of two indices (*i.e.*, $\delta_{ij} = 1$ if $i = j$, and $\delta_{ij} = 0$ if $i \neq j$), whereas $\otimes$ denotes the tensor product, a mathematical operation used to combine two tensors. Within this notion, the plastic deformation is precisely characterized as a strain that occurs without any accompanying stress. However, the Green strain tensor E is extremely important in measuring the extent of elastic strain. To calculate the elastic strain, we can use the Green strain tensor E. Hence, the Green strain tensor can be represented by the equation provided below:

$$E = \frac{1}{2}\left(C - C_p\right) = \frac{\delta_{kl}}{2}\left(F^k_i F^l_j - \left(F_p\right)^k_i \left(F_p\right)^l_j\right) dx^i \otimes dx^j. \tag{3. 3}$$

It is important to emphasize the elastic deformation corresponds to the process of incorporating the intermediate state $\mathcal{B}$ to Euclidean space. In order to achieve the current condition $\mathcal{S}$, we minimize the elastic strain energy.

3.2.2. Cartan first structure equation

We define the intermediate state $\mathcal{B}$ as the Weitzenböck manifold. Here, we may determine the intermediate state by utilizing the dislocation density tensor [7]. As per Nye's theory, the dislocation density tensor is the mathematical concept that describes the continuous arrangement of dislocations [22]. For this situation, we may confidently use the dislocation density tensor α to model dislocations. This tensor is determined by combining the Burgers vector $b\ \partial/\partial x^i$ and the dislocation line tangent vector $n^j \delta_{jk} dx^k$. This allows us to accurately represent the dislocations.

$$\alpha = f b^i n^j \delta_{jk}\, dx^k \otimes \frac{\partial}{\partial x^i}. \tag{3. 4}$$

Here, the dislocation density distribution function is defined by f. By linking the dislocation density tensor α to the continuum kinematics discussed before, we may utilize the equivalence between the torsional form and the dislocation density tensor α, as documented by Kondo [7]. To be more specific, the torsional form τ of the intermediate state $\mathcal{B}$ and the dislocation density tensor α are linked together through the Hodge star operator * [6],

$$\tau =* \alpha = f b^i n^j \epsilon_{jkl}\, dx^k \wedge dx^l \otimes \frac{\partial}{\partial x^i}, \tag{3. 5}$$

where ϵ_{jkl} is the fully antisymmetric tensor. Yavari and Goriely, as well as Kobayashi and Tarumi, have previously shown that the torsion 2-form τ is connected to the plastic deformation gradient. It can be stated as follows:

$$\tau^i = \frac{\partial \left(F_p\right)^i_j}{\partial x^k}\, dx^k \wedge dx^j, \tag{3. 6}$$

Next, we derive the specific equations to be solved. By applying the exterior derivative operator d to the dual frame ϑ^i defined in Equation (3. 1), we obtain the formula $d\vartheta^i = \frac{\partial (F_p)^i_j}{\partial x^k}\, dx^k \wedge dx^j$. Comparing this expression with equation (3. 6), we have the following form

$$\tau^i = d\vartheta^i, \tag{3. 7}$$

Equation (3. 7) represents a mathematical formula of the Cartan first structure equation. In the earlier investigation conducted by Kobayashi and Tarumi, they were able to effectively solve the problem utilizing the homotopy operator [23]. However, if the dislocation arrangement for a kink deformation is less symmetrical, this method cannot be employed. Thus, finite element analysis is employed to numerically solve the equation.

3.2.3. Stress equilibrium equation

After successfully solving the Cartan first structure equation, we move on to the elasticity equation. The Green strain tensor E, as calculated in Equation (3. 3) measures the value of the elastic strain. In our analysis, we confidently assume that the St. Venant-Kirchhoff hyperelastic material incorporates the elastic strain energy of the continuum, thus expanding the concept of linear elasticity into a nonlinear elasticity. Therefore, we express the strain energy functional in the following manner

$$W[y, \vartheta] = \int_{\mathcal{R}} \frac{1}{2} C[\vartheta]^{ijkl}\, E[y, \vartheta]_{ij}\, E[y, \vartheta]_{kl}\, v[\vartheta]. \tag{3. 8}$$

Here, $C[\vartheta]^{ijkl}$ represents the elastic coefficients, whereas $[\vartheta] = (\det \vartheta)\, dx^1 \wedge dx^2 \wedge dx^3$ denotes the volume form. In order to simplify the analysis, we use elastic isotropy for the elastic coefficients. Moreover, we may represent elastic deformation by utilizing the variational principle of hyperelastic material. The strain energy functional is minimized by evaluating the stationary condition, $\delta W = 0$. Let's assume that $(h^i) = (h^1, h^2, h^3)$ represents the test function, which fullfills the constraint $h^i = 0$ on the Dirichlet boundary. Thus, we can articulate the stationary state in the following manner

$$\int_{\mathcal{R}} C[\vartheta]^{ijkl}\, \delta_{mn} \frac{\partial h^m}{\partial x^i} \frac{\partial y^n}{\partial x^j}\, E[y, \vartheta]_{kl}\, v[\vartheta] = 0, \tag{3. 9}$$

Equation (3. *9*) represents the stress equilibrium equation, and is an important component of the geometric theory of dislocations used to explain elastic deformation. In order to answer this equation, we can confidently utilize the finite element approach and numerically solve equation (3. 9).

3.2.4. Modeling kink deformation using dislocation-based approach

Based on the research conducted by Hess and Barret, we have successfully created a deformation model called the ortho kink deformation model, which utilizes arrangements of edge dislocations [14]. Here is an overview of the kink models used in this work, as shown in Figure 3. 1. These models are in the form of rectangular parallelepipeds with normalized dimensions: $L_1/b = 4{,}000$, $L_2/b = 1{,}000$ and $L_3/b = 1{,}000$, where b represents the Burgers vector magnitude. Here, we develop two models to examine the growth mechanism of kink interface, as depicted in Figure 3. 1. Model I demonstrates a scenario in which the kink interface expands from one side of the model, keeping an equal length. On the other hand, Model II exhibits a situation when the kink interface expands from opposing directions while maintaining a consistent length. The parameter H, ranging from 0 to L_3, denotes the length of the kink interface expansion. Since the dislocation of the two kink interfaces has different signs, it may be inferred that the bending angle θ at the interfaces is similarly opposite. Once the kink interfaces, $H = L_3$, are fully developed, both models produce the same deformation microstructure known as ortho-kink. While the final microstructure will stay consistent, we expect to see a noticeable variation because of the disclinations present at the tip of the kink interfaces.

We used the continuous distribution theory of dislocations to model the planar arrangement of edge dislocations on a kink interface. To be more specific, the dislocation density is determined by utilizing the level-set function. We consider f as the dislocation density funstion and d as the distance from the kink interface center. To keep things simple, we will assume that the dislocation density follows a linear distribution, which can be characterized by the following form:

$$f(d) = \begin{cases} \frac{1}{RH}\left(1 - \frac{d}{R}\right) & d \leq R \\ 0 & d > R \end{cases}. \tag{3. 10}$$

Here, R is the radius of the dislocation core, whereas $1/RH$ is used as the coefficient for normalization. As seen in Figure 3. 1, the arrangement of the dislocation closely mimics that of a tilt grain boundary as the kink interface expands considerably. When the ortho-kink fully penetrates the material, meaning $H = L_3$, it causes a finite bending deformation θ at the interface. The bending angle θ may be associated with the Burgers vector magnitude and the distance between the dislocations at the kink interface, referred to as h, as expressed by [1, 15]

$$\tan\theta = \frac{b}{h}. \tag{3. 11}$$

We use the finite element method to perform numerical analysis. At first, we allocate 300 meshes for the x_1 direction, 10 meshes for the x_2, direction, and 75 meshes for the x_3 direction. This gives us a total of 225,000 meshes. Nevertheless, this degree of freedom is not enough to achieve accurate numerical results. As a result, we do local mesh refinement, especially around the kink interfaces. This leads to a total of 8 million degrees of freedom in the numerical analysis. In addition, boundary conditions are crucial when it comes to modeling kink deformation. In order to obtain precise measurements of the stress field caused by kinked deformation, it is important to reduce any mechanical limitations that may arise from the boundary conditions. Therefore, we assign a Neumann boundary condition that is free of traction to almost all planes in the simulation area. However, in order to avoid any movement in a straight line, displacements are restricted to zero on the $x_1 = 0$ plane. For this numerical study, we set $b = R = 1$, which means that the dislocation core radius is equal to the magnitude of the Burgers vector. Furthermore, the stress S_{ij} is appropriately normalized by dividing it by the shear modulus, which is represented as $S_{ij} \rightarrow S_{ij}/G$. Likewise, we can normalize the strain energy by dividing it by the product of the Young modulus and the magnitude of the Burgers vector. This can be expressed as $W \rightarrow W/(Eb^3)$.

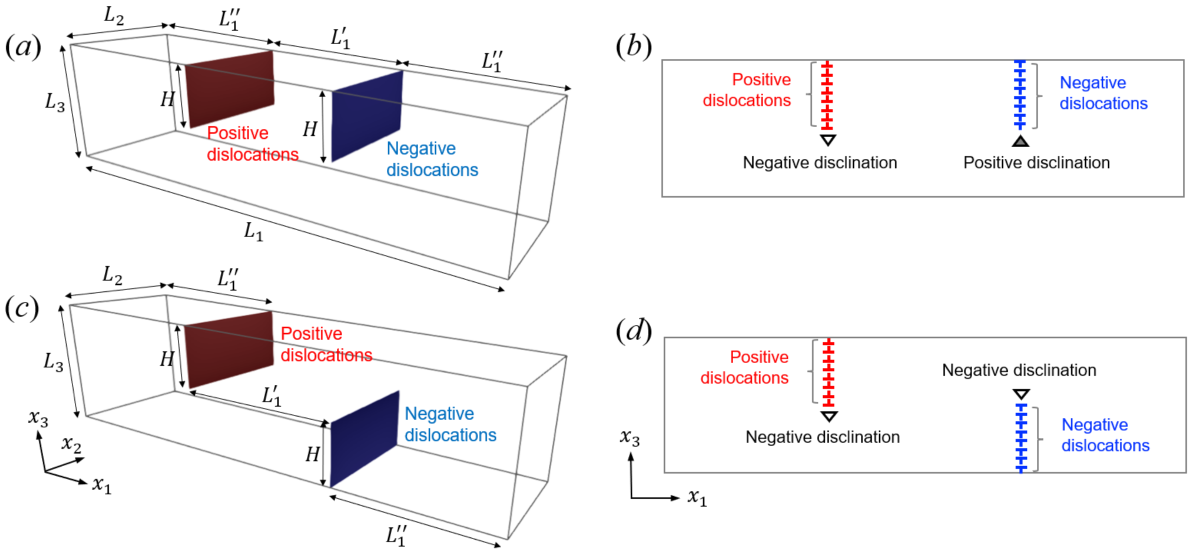

Figure 3. 1 depicts the dislocation model in ortho kink deformation, with the following dimensions: $L_1/b = 4{,}000$, $L_2/b = 1{,}000$, and $L_3/b = 1{,}000$. (a) illustrates Model I, in which kinnk interface grows from the same side. Subsequently, disclinations with opposite signs will develop, as depicted in (b). (c) describes Model II, which elucidates the growth of the kink interface from opposing directions. In (d), a disclination emerges at the termination of the kink interface, exhibiting identical form.

3.3.Numerical analysis results for kink

3.3.1. Validation of the ortho kink deformation

Our kink model, as depicted in Figure 3. 1, consists of two kink boundaries that have arrays of edge dislocations, both positive and negative. Let's emphasize that we can vary the length of the kink boundaries, which is designated as H, to better comprehend the process of ortho-kink growth. Therefore, this part will mainly concentrate on doing an initial quantitative validation of our kink model by analyzing the whole growth state.

Figure 3. 2(a) shows an illustration of elastoplastic deformation obtained using numerical analysis. The parameters used are $h = 10b$, $L_1' = L_1'' = L_1/3$, and $H = L_3$. The color representation indicates the amount of displacement from the initial state. Clearly, it is evident from the figure that the region on the left, which spans from $0 < x_1 < L_1/3$, shows minimal change. By applying the Dirichlet boundary condition on the $x_1 = 0$ plane, we ensure

that there are no stiff body movements allowed in the model. Similarly, the next one-third section $(2L_1/3 < x_1 < L_1/3)$ only shows rigid body movement along the x_3 axis. This suggests that there are no mechanical restrictions on kink deformation caused by the boundary conditions. On the other hand, the magnitude of displacement is evenly distributed throughout the kink interfaces. This unique deformation pattern occurs only when the kink interfaces experience sharp bending. This result clearly shows the overall shape that is similar to the ortho-kink seen in observations [14].

According to the lattice defects theory, a planar array of edge dislocations creates a tilt grain boundary. The bending angle of this model is given by Equation (3. 11). This relationship is employed to quantitatively validate the present model. Figure 3. 2(b) displays the association between the bending angle θ at the kink interfaces and the dislocation distance, which is normalised by the Burgers vector, h/b. The FEM analysis findings are represented by the solid circles, while the theoretical prediction derived from Equation (3. 11) is represented by the solid curve. The outcome demonstrates a satisfactory level of concurrence with a minor variation of under 13%. There are a few causes that could be causing this small divergence from the theoretical expectations. These factors are mostly related to possible flaws in the calculations. In general, while doing three-dimensional analysis, a significant number of degrees of freedom are required, especially around the kink interfaces. Although we conducted the present investigation with 8 million degrees of freedom, it is possible that the analytical precision may still be insufficient.

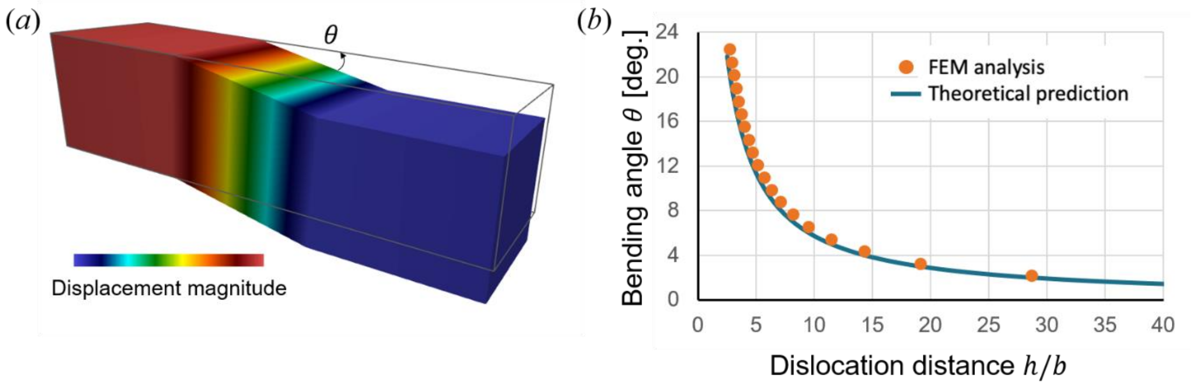

Figure 3. 2(a) shows the macroscopic deformation of the ortho kink model. Obviously, there is a bending deformation surrounding the kink interface. The bending angle (b) is determined using FEM analysis and it aligns quantitatively with the theoretical predictions, as described in Equation (3. 11).

3.3.2. Strain Energy

The ortho kink model has shown numerous crucial aspects. Firstly, it is clarified that the pronounced bending deformation at a kink interface corresponds precisely to the Hess and Barret model [14]. The outcome strongly indicates that the kink deformation originates from a planar arrangement of edge dislocations. Thus, it is logical to propose that the onset of kink formation is preceded by the generation of dislocation loops within an ideal crystal. Nevertheless, the nucleation process may not be suitable for investigation using continuum mechanics and may be more appropriate for atomic-level simulations such as molecular dynamics. On the other hand, studying the energy and stress distribution in the growth process is important in macro-scale analyses that use continuum mechanics. Multiple tests have demonstrated that the kink interface expands during plastic deformation. However, understanding the strain energy and the accompanying internal stress state is still a challenge, as it necessitates nonlinear elastoplastic analysis. The increase in strain energy associated with kink growth corresponds to the external work required for plastic deformation to occur. Essentially, it denotes the ability of a substance to withstand deformation. This quantitative analysis is important for comprehending the mechanics underlying material strengthening. Therefore, the strain energy generated during the formation of a kink becomes essential. Consequently, we will continue by making further measurements, namely measuring the amount of strain energy in the material due to the length of the kink interface (H) and the distance between kinks (L_1').

At first, we made modifications to the kink interfaces (H) in the region of 0 to L_3, with an increase of $\Delta H = L_3/10$ for Model I. Concerning the distance between kinks, we set $L_1' = L_1/3$ and $L_1' = L_1/12$. Figure 3. 3(a) depicts the strain energy associated with the length of the kink interface, denoted as H. This figure illustrates the external work required to expand the kink interface within Model I. This outcome demonstrates that the energy exhibits nearly perfect symmetry in relation to the length H and reaches its highest value at $H/L_3 = 0.5$. This energy is represented as the pivotal energy point. More precisely, if the magnitude of the external effort does not exceed this critical point, the kink can only expand until it reaches a position that is counterbalanced by the applied external force. Exceeding this critical energy point leads to the expansion of the interface, resulting in the formation of a microstructure characterized by ortho-type kinks. Therefore, kink deformation can be understood as being similar to a plastic buckling process characterized by mechanical instability. Figure 3. 3(b) exhibits comparable outcomes derived from Model II, illustrating the same pattern as shown in Figure 3. 3(a) with the highest level of strain energy attained at $H/L_3 = 0.5$. In Model I, an increase in energy levels is observed when the distances between the kink interfaces L_1' become longer. On the other hand, in Model II, higher energy is linked to shorter L_1' distances.

The analysis based on disclination is of significant value. According to the lattice defect theory, it is established that a wedge disclination occurs at the end of a row of edge dislocations [15]. Therefore, when examining the dislocation arrangement shown in Figure 3. 1, it can be observed that two wedge disclinations appear at the ends of the internal dislocation rows within the material (refer to Figure 3. 1(b) and (d)). Model I contains two wedge disclinations of opposite signs, while Model II contains two wedge disclinations of the same sign.

When the disclination signs are similar, they repel each other elastically, resulting in an increase in strain energy as the distance between the kink interfaces, L_1' ', decreases. In contrast, disclinations with opposite signs demonstrate elastic attraction, leading to a reduction in strain energy as the distance between kink interfaces, denoted as L_1', increases. This elucidates the disparity in energy levels between (a) and (b) in Figure 3. 3, which corresponds to alterations in L_1'. Furthermore, the energy profile is also affected by the existence of the free surface. According to Figure 3. 2, when the kink interface is not well developed (i.e., when H is small), the disclination is located close to the surface, leading to a lower amount of strain energy. In contrast, when the disclination is of significant magnitude, it moves to the surface that is opposite to its original position, leading to a decrease in strain energy as well. As a result, the self-energy of the disclination is maximized at $H/L_3 = 0.5$, which corresponds to the point farthest away from the surfaces. Therefore, the energy profile of kink growth is determined by two main factors: the elastic interaction energy and the self-energy of disclinations. The energy barrier functions as a mechanism that enhances the strength by requiring more effort to enable the deformation of the material. The strengthening of the material caused by kink deformation can be attributed to the creation of a disclination at the end of the kink interface growth front.

Another important conclusion derived from the results highlights the strong reliance of the external effort required for kink deformation on the process of kink growth. This emphasizes that it cannot be determined purely based on the shape of the kink deformation. As previously mentioned, although the kink deformation shapes in both models look the same when $H/L_3 = 1.0$, there is a considerable difference in the amount of external work needed. For instance, when the inter-kink distance is reduced to $L_1' = L_1/12$, the strain energy between the two models varies by a factor of 2.7. The variation occurs as a result of the elastic interaction energy between the disclinations. In contrast, when the distance between the kinks is greater, the strain energies of the two models almost coincide. Therefore, the elastic interaction between kinks remains present to a distance of $L_1' = L_1/12$, but decreases at a distance of $L_1' = L_1/3$.

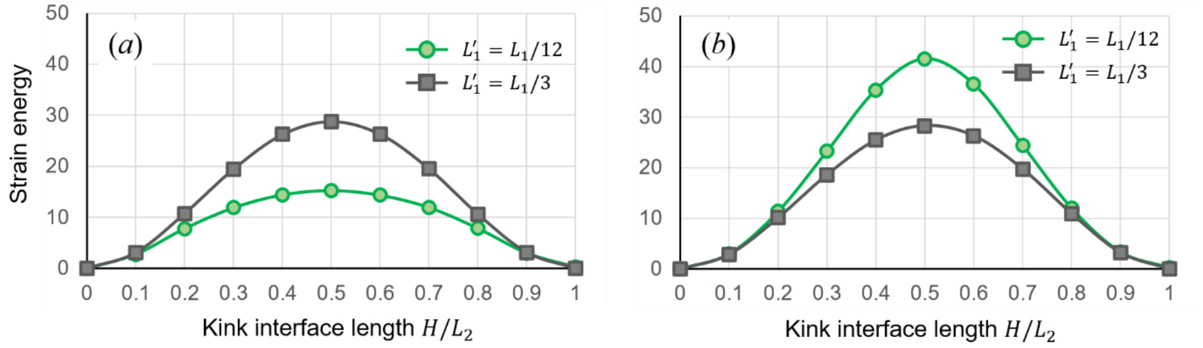

Figure 3. 3(a) displays the strain energy acquired from Model I, whereas (b) represents the strain energy derived from Model II. In Model I, the strain energy decreases as the kink interfaces are closer together. In contrast, in Model II, the strain energy increases because disclinations with the same sign are in close proximity. It should be noted that the strain energies are normalized by Eb^3.

3.3.3. Analysis of stress fields resulting the disclinations

In the previous part, it was observed that when the kink interface length $H/L_3 = 0.5$, it results in the maximum amount of strain energy due to the creation of wedge disclinations. An important and fascinating question arises regarding the nature of the internal stress field that is accountable for this state of maximal strain energy. In other words, what kind of internal stress field forms near the wedge disclination at the growing front of the kink interface? Nevertheless, this investigation has not been thoroughly examined due to many factors. Prior research on disclination have predominantly utilized linear elasticity in their observations, in contrast to the current work which is based on nonlinear elasticity. Linear elasticity is based on the assumption of extremely small deformations, which means it cannot analyze a finite angular change θ caused by kink deformation. Furthermore, concerns arise with the occurrence of stress singularity

In traditional classical lattice defect theory, it is assumed that there is an infinite increase in stress at the centre of a lattice defect. This is analysed using the Dirac delta function [2, 1]. Unlike previous studies, the current research utilises a continuous level set function to depict the dislocation array. This approach prevents the occurrence of stress singularities during the analysis. The ultimate obstacle is the limitations imposed by boundary circumstances. Traditional models of lattice defects typically focus on examining stress distributions in infinite structures, often neglecting finite systems that include free surfaces. As previously shown, the presence of free surfaces has a substantial impact on the amount of strain energy, and this applies to real-world materials as well. It is anticipated that the stress field will display distinct distributions on the surface and in the inside. Hence, it is imperative to do a stress field analysis within a limited area that includes free surfaces.

Figure 3. 4 illustrates the distribution of the second Piola-Kirchhoff stress S_{ij} obtained from Model I with a ratio of $H/L_3 = 0.5$ and $L'_1 = L_1/3$. Notably, we set $h/b = 5.6$, indicating a bending angle of approximately $\theta \sim 10°$. Figure 3. 4 (a), (b), and (c) depict the normal stress components, whereas panels (d), (e), and (f) exhibit the shear stresses. It becomes apparent that the three normal stresses, namely S_{11}, S_{22} and S_{33}, concentrate around the termination point of the kink interface, rather than dispersing across the surface. Furthermore, their arrangement in the cross-sectional direction highlights significant stress concentration along the x_3 axis, which coincides with the growth front of the kink interface. The absolute values of the normal stress components are almost ten times more than the remaining three shear stress components. This suggests that the normal stresses have a dominant influence on the disclination's self-energy. Regarding shear stresses, the S_{23} component exhibits minimal values, which are only found at the free surface. On the other hand, the S_{12} component remains consistently tiny throughout the entire material. Therefore, the impact of these two shear stresses on the strain energy seems insignificant. In contrast, the S_{13} component has significant values that are spread out over the model. Therefore, S_{13} plays a role in the long-distance interaction between the disclination and other defects in the lattice.

Figure 3. 5 depicts the distribution of elastic stress fields obtained from Model I when H/L_3 is equal to 0.5 and $L'_1 = L_1/12$. There is no change in stress distribution since the shape of the kink deformation remains the same; only the distance between kinks is modified. The typical stress components shown in Figure 3. 5(a), (b), and (c) closely mirror those in Figure 3. 4, but there are noticeable quantitative differences. For example, there is a decrease in the distribution of normal stresses combined with lower values of maximum stress. These changes arise from the interaction of disclinations. Figure 3. 1(b) and (d) illustrate the presence of two wedge disclinations with opposite signs at the kink interface tip. In Figure 3. 4, the normal stresses in their vicinity display opposite signs. As a result, when these disclinations get closer together, their stress fields cancel each other out, resulting in a decrease in strain energy. This immediately leads to a reduction in the energy barrier associated with the distance between the disclinations (see Figure 3. 3 (a)). Similarly, there are no substantial changes in the two shear

stress components, S_{23} and S_{12}. On the other hand, it is unexpected that the shear stress S_{13} between the disclinations of the same sign actually increases the elastic strain energy due to their interactions. However, when compared to the typical stress, the magnitude of S_{13} remains minimal and therefore does not have a substantial effect on the energy barrier.

Figure 3. 6 and Figure 3. 7 provide an overview of the stress fields that were obtained from Model II. The disclinations created at the growing front of the kink interface show the same signs, as shown in Figure 3. 1(b) and (d). As a result, the stress fields around these disclinations also show the same signs. The strain energies derived from Model II at the distance $L_1/3$ roughly correspond to the results of Model I, as shown in Figure 3. 4(a) and (b). This discovery implies that the distance $L_1/3$ separating disclinations is sufficiently large, resulting in the elastic interaction between them being insignificant. On the other hand, when the distance between kink interfaces is decreased, it causes the wedge disclinations to repel each other, resulting in an increase in strain energy. Moreover, Figure 3. 7 elucidates that this extra energy mostly originates from the contribution of the normal stressS_{11}.

The investigation of the stress field offers numerous important results regarding the energy dynamics of the process of kink formation. Initially, the strain energy resulting from the inter-kink distance $L_1' = L_1/3$ mostly consists of the self-energies of the two disclinations. This represents a typical energy barrier for unrestricted kink growth, without any elastic interaction with other defects. To overcome this energy barrier, an external force is required to enable plastic deformation, which ultimately determines the strength of kink-deforming materials such as LPSO Mg alloys. Nevertheless, the energy barrier is significantly dependent on the nearby microstructure because of the elastic interactions between disclinations at the kink contacts and other defects. Hence, the energy barrier for plastic deformation might vary considerably depending on the formation process, although having similar final kink microstructures. Simply said, relying merely on the resulting kink microstructure after deformation is inadequate for deducing the resistance to plastic deformation. Furthermore, the shear stress component S_{13} plays a prominent role in the elastic interaction between disclinations and other defects. It shows a wide distribution over a distance of approximately 1,000b. The Peach-Koehler force acting on a dislocation, as described by classical dislocation theory, can be mathematically represented as $F_k = t_j \times \left(\sigma_{ij} b_j\right)$, where t_j, σ_{ij}, and b_j respectively represent the tangent direction, linearized Cauchy stress, and Burgers vector of the dislocation. The symbol × denotes the outer product. By making the simplifying assumption that the second Piola-Kirchhoff stress S_{ij} is equal to the linearized Cauchy stress σ_{ij}, we can observe that the shear stress fields S_{13} interact with dislocations that have Burgers vectors parallel to the x_3-axis. This approach is particularly fascinating when considering a hexagonal lattice. The kink deformation in a hexagonal crystal is caused by the glide motion of a-type edge dislocations on the basal plane, as stated earlier. In this situation, these dislocations arrange themselves into arrays to create the kink interface, with the Burgers vector $(b, 0{,}0)$ specifically on the x_3 plane. Hence, the S_{13} stress interacts with c-type dislocations that are not in the same plane in the hexagonal lattice. Recent investigations have documented the emergence of c-type dislocations on kink interfaces, maybe associated with the disclination shear stress.

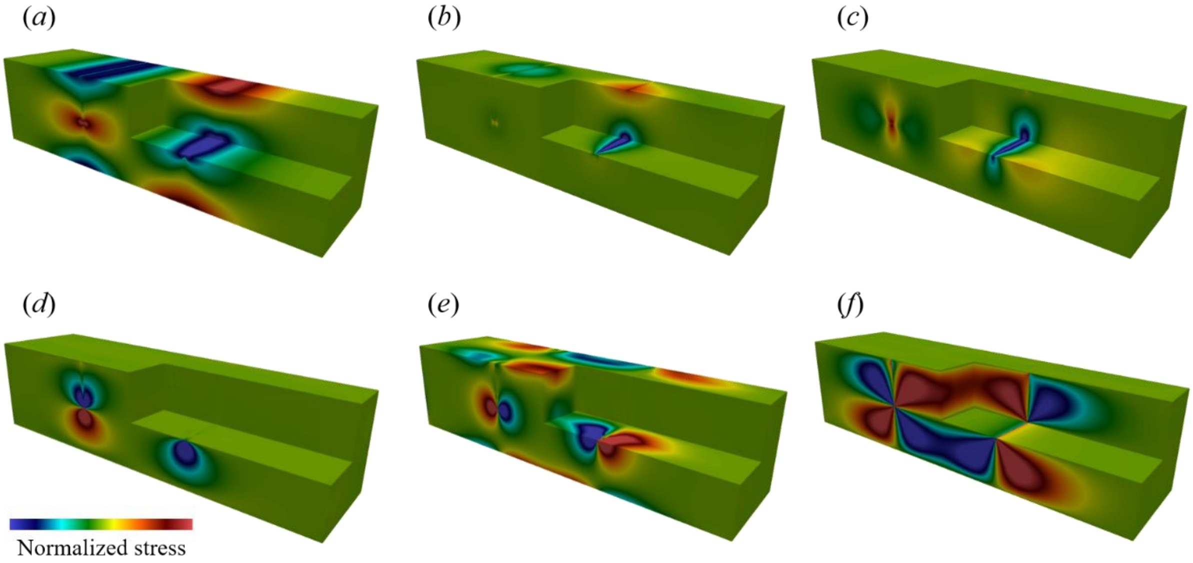

Figure 3. 4 shows the distribution of second Piola-Kirchhoff stress S_{ij} generated from Model I with $H/L_3 = 0.5$ and $L_1' = L_1/3$. The normal stress components S_{11}, S_{22}, and S_{33} are depicted in (a), (b), and (c), respectively. Meanwhile, (d), (e), and (f) depict the dispersion of the shear stress fields.

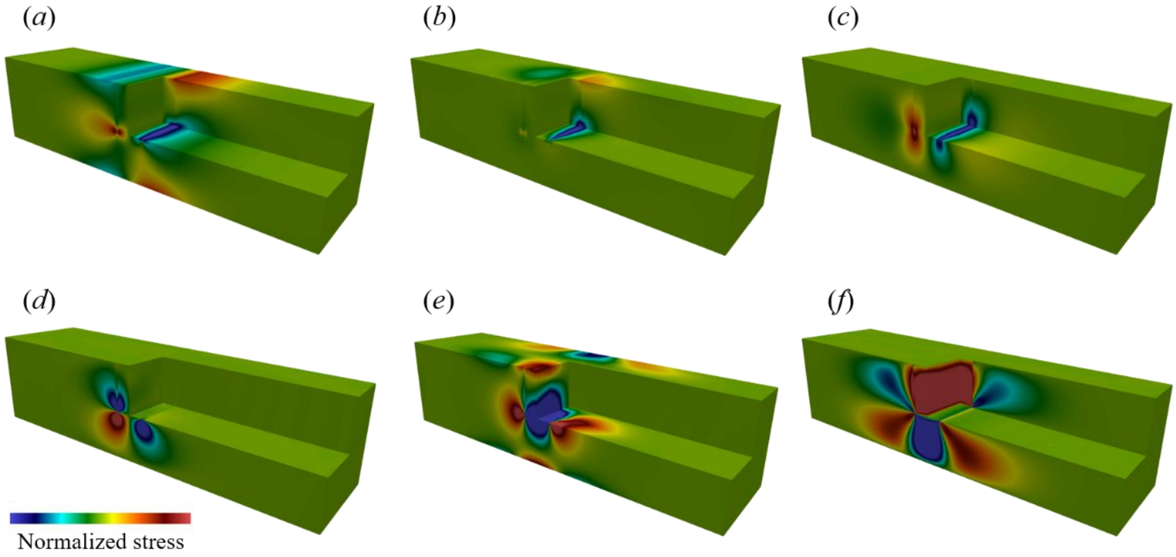

Figure 3. 5 shows the distribution of second Piola-Kirchhoff stress S_{ij} generated from Model I with $H/L_3 = 0.5$ and $L_1' = L_1/12$. The normal stress components S_{11}, S_{22}, and S_{33} are depicted in (a), (b), and (c), respectively. Meanwhile, (d), (e), and (f) depict the dispersion of the shear stress fields.

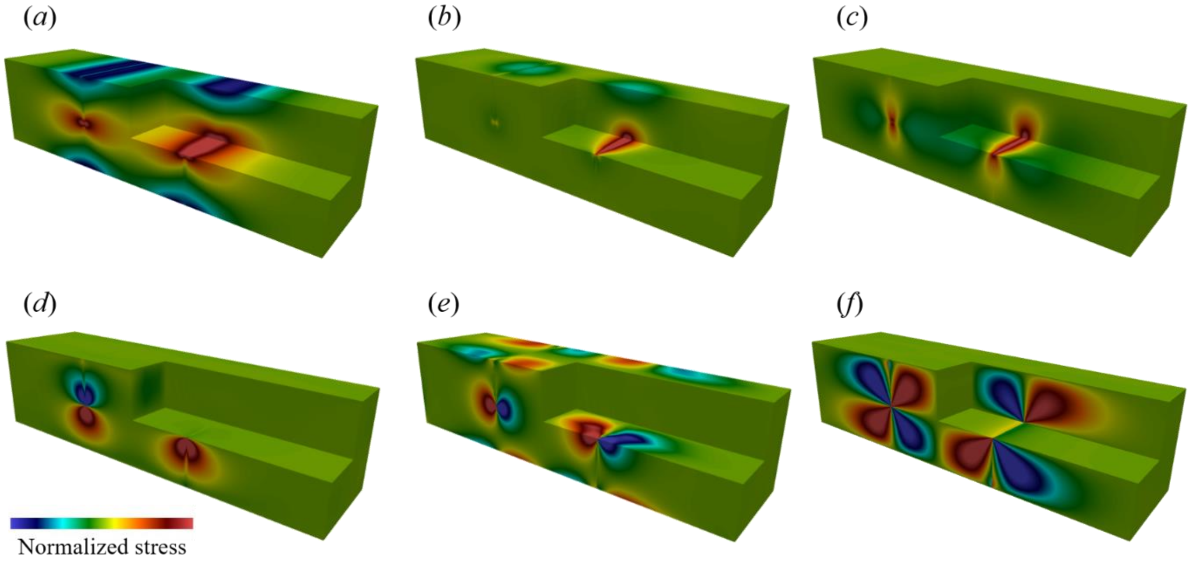

Figure 3. 6: shows the distribution of second Piola-Kirchhoff stress S_{ij} generated from Model II with $H/L_3 = 0.5$ and $L_1' = L_1/3$. The normal stress components S_{11}, S_{22}, and S_{33} are depicted in (a), (b), and (c), respectively. Meanwhile, (d), (e), and (f) depict the dispersion of the shear stress fields.

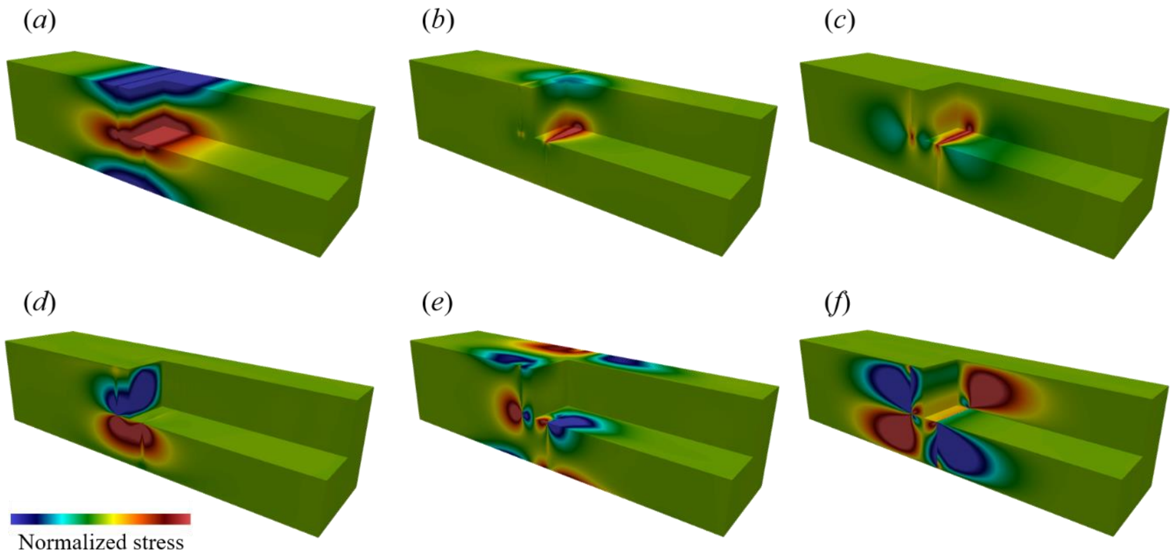

Figure 3. 7 shows the distribution of second Piola-Kirchhoff stress S_{ij} generated from Model II with $H/L_3 = 0.5$ and $L_1' = L_1/12$. The normal stress components S_{11}, S_{22}, and S_{33} are depicted in (a), (b), and (c), respectively. Meanwhile, (d), (e), and (f) depict the dispersion of the shear stress fields.

.

Chapter IV

Investigation of the Presence of Disclinations in Ridge Kink Deformation Through Quantitative Analysis

4.1. Research background

Layered structures are abundant in nature at different scales [24]. Examples include a wide range of materials such as wood [25] and rocks [26], and are commonly seen in composite materials, regardless of whether they are made of metal or non-metal [27, 28, 29, 30, 31, 32, 33]. These materials, renowned for their stratified microstructures, have garnered considerable attention, specifically magnesium alloys that incorporate the LPSO phase [11]. LPSO Mg alloys are widely recognized for the outstanding mechanical characteristics, such as high-yield strength and reasonable plastic elongation [11, 34]. Initially, the increase in mechanical characteristics was ascribed to a reduction in particle dimensions. However, it is becoming clear that the existence of the LPSO phase significantly contributes to the improvement of its mechanical characteristics [10, 35]. LPSO structures are mostly formed by introducing Zn and rare earth metals into magnesium alloys, which are subsequently distributed throughout the hexagonal crystal lattice [37, 38]. Unlike traditional alloys, the LPSO structure exhibits a distinctive characteristic of kink production during the process of deformation. The extraordinary strength characteristics are associated with a special type of plastic deformation called kink deformation [35, 39, 40]. Several investigations have been carried out to understand the mechanism of strengthening, using methods such as grain size modifications and double compression tests with different loading orientations [41-44]. Nevertheless, the specific process by which kink deformation improves material characteristics is still not fully understood.

In the 1940s, Orowan first noticed kink deformation on his experiments [13]. Experimental investigation revealed that subjecting a Cd single crystal to uniaxial compression along the basal plane led to kink deformation. Additional evidence for this discovery was provided by Jillson and Gilman [19, 20], who verified the occurrence of kink deformation when subjected to compressive pressure. This phenomenon was observed not only in Cd single crystals but also in other materials such as Zn single crystals. This finding confirmed the notion that materials with a layered microstructure are susceptible to experiencing kink deformation due to uniaxial compression. Hess and Barret subsequently proposed the dislocation-based kink deformation theory [14], indicating the formation of kink band occurs through the interaction of edge dislocations arrangements with opposing signs interact with one other. Nevertheless, their model was unable to completely elucidate the observed augmentation in material strength linked to kink deformation. Recent research on kink deformation has revealed that disclinations are crucial in improving the mechanical characteristics experiencing kink deformation [21]. However, disclinations did not receive much focus until Nabarro emphasized the crucial significance in the deformation mechanism of layered materials. [45].

Volterra subsequently introduced the notions of dislocations and disclinations to the theory of elasticity [2]. Prior research has shown that disclinations disclinations result in notable stress concentrations and can impede the movement of dislocations [46, 48, 49]. Here, the kink bands act as barriers to additional deformations [21]. Furthermore, it has been hypothesized that disclinations occur at the terminations of kink bands, when the kink bands are incapable of penetrating the material [16]. Nevertheless, there is a lack of extensive research on disclinations, which makes it difficult to accurately verify their existence in kink deformation using quantitative methods. Quantitative confirmation of disclinations requires the Frank vector measurement that signifies the intensity of disclinations [46]. Nazarov et al. conducted a theoretical investigation to determine the misorientation angle in tilt grain boundaries. Nevertheless, they failed to discuss the method for quantifying the intensity of disclinations, as indicated by the Frank vector [50].

Despite numerous efforts to prove the existence of disclinations, preciesly determining the Frank vector in any dislocation arrangements still requires careful consideration [51, 21]. An obstacle that affects these measures is that previous investigations were carried out in traditional Euclidean space, neglecting the implications of the Riemann-Cartan manifold [6, 52]. This constraint arises due to the presence of residual tensions in objects containing disclinations. Using the initial configuration, as typically done in conventional space, is insufficient. One way to address this issue is to break down the deformation gradient into elastic and plastic parts at a local level. This involves incorporating differential geometry to effectively model disclinations. Disclinations in Riemannian manifolds are associated with the curvature tensor in differential geometry. Hence, the lack of torsion and curvature tensors in a conventional space makes it inappropriate for disclination modeling. In addition, the holonomy method provides a technique for identifying curvature based on the concepts of differential geometry.

This study aims to identify the existence of disclinations within kink microstructure using measurement of the Frank vector. To accomplish this objective, we propose the utilization of the holonomy technique to assess the Frank vector of disclinations within different dislocationo arrangements.

4.2. Formulation of Lattice Defect Theory Using Differential Geometry

4.2.1. Dislocation Kinematics

The dislocation theory employed in this course adheres to a mathematical framework rooted in the Riemann-Cartan manifold [6, 3]. The mathematical framework states that the motion of a continuous material can be described using three separate configurations: the initial reference configuration $\mathcal{R}$, an intermediate configuration $\mathcal{B}$, and the current configuration $\mathcal{S}$. To be more precise, the reference configuration represents an ideal crystal, the intermediate configuration is a hypothetical state that accounts for a lattice mismatch caused by defects in the lattice and only involves plastic deformation, and the current configuration is a state of mechanical equilibrium that encompasses both plastic and elastic deformations. Thus, these arrangements are linked to the multiplication-based breakdown of the deformation gradient, where $F = F_e \cdot F_p$. Here, F_p and F_e represent the plastic and elastic deformation gradients, respectively.

Consider the line elements in three configurations: $\left(dx^i\right) = (dx^1, dx^2, dx^3)$, $\left(\vartheta^i\right) = (\vartheta^1, \vartheta^2, \vartheta^3)$, and $\left(dy^i\right) = (dy^1, dy^2, dy^3)$. The Riemannian metrics g_R, g_B and g_S can be defined in three different configurations using linear transformations.

$$\begin{gathered} g_R = \delta_{ij}\, dx^i \otimes dx^j, \quad g_B = \delta_{ij} \left(F_p\right)^i_k \left(F_p\right)^j_l\, dx^k \otimes dx^l, \\ g_S = \delta_{ij} (F_e)^i_k (F_e)^j_l\, dx^k \otimes dx^l. \end{gathered} \tag{4. 1}$$

In this context, δ_{ij} and $\otimes$ denotes the Kronecker and the tensor product, respectively. The magnitude of elastic strain in the present state could be determined according to equation above, using the Green strain tensor E. It is calculated as the discrepancy between the Riemannian metrics in the current and intermediate states, as shown in the following equation.

$$E = \frac{1}{2}(g_S - g_B) = \frac{\delta_{ij}}{2}\left((F_e)^i_k (F_e)^j_l - \left(F_p\right)^i_k \left(F_p\right)^j_l\right) dx^k \otimes dx^l. \tag{4. 2}$$

In addition, the elastic strain is derived from the mapping of the intermediate configuration to the conventional space by minimizing the strain energy.

4.2.2. Determination of the plasticity equation

In the theory formulated by Nye [22], it has been suggested that dislocations can be represented using the dislocation density tensor α. This tensor is defined as the result of multiplying the Burgers vector $b^i \frac{\partial}{\partial x^i}$ with the dislocation line tangent vector $n^j \delta_{jk} dx^k$.

$$\alpha = f b^i n^j \delta_{jk} dx^k \otimes \frac{\partial}{\partial x^i}. \tag{4. 3}$$

In this context, the function f denotes the dispersion of dislocation density. In addition, Kondo [7] noted that the dislocation density tensor α in solid mechanics is equivalent to the torsion 2-form τ in differential geometry when the Hodge star operator * is applied, such that $\tau = * \alpha$.. To be more exact, we possess

$$\tau = * \alpha = \left(f b^i n^l \epsilon_{ljk}\right) dx^j \wedge dx^k \otimes \frac{\partial}{\partial x^i}, \tag{4. 4}$$

The symbol ϵ_{ljk} represents a permutation tensor. Furthermore, this torsion also implies that the dislocation density can be distributed in any manner in relation to this characteristic. Previous studies [6, 3] have previously demonstrated that the torsion 2-form τ is connected to the plastic deformation gradient F_p in a specific manner.

$$\tau^i = \frac{\partial \left(F_p\right)^i_j}{\partial x^k} dx^k \wedge dx^j. \tag{4. 5}$$

Similarly, from the local coordinate system in the intermediate configuration, we have the relation $\vartheta^i = \left(F_p\right)^i_j dx^j$. Thus, it can be stated that the Cartan first structure equation can be expressed in the following form

$$\tau = d\vartheta. \tag{4. 6}$$

Here, d stands for the exterior derivative operator. In accordance with our research group [53], the homotopy operator has been successfully used to solve Equation (4. 6). However, it is not suitable for cases with lower symmetry, such as kink deformation. Hence, the finite element method is employed to numerically solve Equation (4. 6).

4.2.3. Elasticity equation

Let y be a continuous function that maps the intermediate $\mathcal{B}$ to the current $\mathcal{S}$ configurations, meaning it embeds the Riemann-Cartan manifold into Euclidean space. The mapping of this embedding can be described as elastic deformation, and the magnitude of this deformation can be quantified using the Green strain tensor, as defined by Equation (4. 2). Additionally, we posit that the elastic strain energy of the continuum is characterized by the St.

Venant-Kirchhoff hyperelastic material. Thus, we can express the strain energy functional for the material that demonstrates kink deformation as follows.

$$W = \int \frac{1}{2} C^{ijkl} E_{ij} E_{kl} \det F_p dV. \tag{4. 7}$$

Furthermore, it is feasible to ascertain the state of equilibrium for the strain energy functional described in Equation (4. 7) by applying the variational principle of hyperelastic material in a manner that ensures that $\delta W = 0$. Let $(h^i) = (h^1, h^2, h^3)$ denote the trial function that fulfills the case $h^i = 0$ on the Dirichlet boundary. Thus, the need for the system to be in a stationary state can be formulated as

$$\int C^{ijkl} \delta_{mn} \frac{\partial h^m}{\partial x^i} \frac{\partial y^n}{\partial x^j} E_{kl} \det F_p \, dV = 0. \tag{4. 8}$$

This equation is referred to as the stress equilibrium equation. In the geometrical dislocation theory, the weak form equation is employed to calculate elastic deformation.

4.2.4. Measurement of Frank vectors using the holonomy approach

In order to prove the existence of disclinations, we employed the holonomy technique, which is a concept derived from differential geometry. This approach is employed to measure the Frank vector, which serves as an indicator of the strength of disclinations [46]. Disclinations are regarded as curvature tensors in accordance with the geometric theory of defects [6, 52]. Evaluating the curvature would verify the presence of disclinations. In order to do curvature analysis, we build a Riemannian manifold that demonstrates non-zero curvature. Here, the holonomy approach offers a means to ascertain and quantify curvature.

A crucial element entails utilising the Levi-Civita connection, denoted as Γ_{ij}^k, which provides a relationship for each point in the tangent plane of a closed curve on the Riemannian manifold. This Γ_{ij}^k is derived from the Riemannian metric in the intermediate state and is also related to the plastic deformation gradient F_p. Therefore, the plastic deformation gradient F_p allows for the calculation of Γ_{ij}^k using the Riemannian metric, as specified in Equation (4. 2). Hence, the formulation for the Levi-Civita connection is stated as follows.

$$\Gamma_{ij}^k = \frac{g^{*kl}}{2} \left(\frac{\partial g_{li}}{\partial x^j} + \frac{\partial g_{lj}}{\partial x^i} - \frac{\partial g_{ij}}{\partial x^l} \right), \tag{4. 9}$$

In order to utilize the holonomy approach for quantifying the Frank vector, the first step entails the identification of a closed surface, referred to as c, within the Riemannian manifold. Next, it is postulated that the closed surface is a Frank circuit. Commencing from a specified point on the Frank circuit, the vector X_s undergoes parallel transport along the Frank circuit until it returns to its original location, obtaining in the vector X_e. The angular disparity between X_s and X_e ultimately corresponds to the holonomy angle, denoted as ω. The translation vector X can be obtained by solving the equation below [54]:

$$\frac{\partial X^i}{\partial t} + \Gamma^i_{jk} \dot{c}^j X^k = 0. \tag{4. 10}$$

The angular disparity between these vectors is computed with the holonomy approach, presumed to represent the Frank vector, resulting in the following expression.

$$\omega = \cos^{-1}\left(\frac{g_{\mathcal{B}}(X_s, X_e)}{\sqrt{g_{\mathcal{B}}(X_s, X_s)}\sqrt{g_{\mathcal{B}}(X_e, X_e)}}\right). \tag{4. 11}$$

Afterwards, the outcomes derived from the holonomy approach is contrasted with the smal-angle grain boundaries theory. [1].

Here, we utilize the finite element approach for our numerical analysis. In order to facilitate this investigation, we construct a 2D square model with a mesh count of 320 in both the x_1 and x_2 axes, yielding a total of around 102,400 meshes. Consequently, there is a need for localized mesh refinement at the kink boundaries. As a results, localized mesh refinement along the kink boundaries and their endpoints, leading to a total number of DOF exceeding 11 million.

4.3. Quantitative verification of the holonomy approach

The verification of the holonomy approach is conducted on several dislocation configurations. This quantitative validation entails the comparison of the numerical analysis derived from holonomy approach with the predictions proposed in the thory of grain boundary [1]. In order to carry out this comparison, a square model with two dimensions is created. The dimensions are normalized and expressed as $L_1/b = 1{,}000b$ and $L_2/b = 1{,}000b$. The notion of continuous dislocation density is used to model an arrangement of edge dislocations on a kink interface. To streamline the study, we use a linear dislocation density distribution as described below:

$$f(x) = \begin{cases} \frac{1}{RL}\left(1 - \frac{d}{R}\right) & d \le R \\ 0 & d > R \end{cases}. \tag{4. 12}$$

Here, R represents the dislocation core radius, whereas L is the length of the kink boundary. The normalized coefficient is given by $1/RL$. Subsequently, we enlarged the region surrounding the kink interface with the intention of quantifying the disclination within this specific area, as shown in Figure 4. 1.

The first dislocation model investigates the situation where the Burgers vector is aligned in the x_1 direction (see Figure 4. 1(a)). The dislocation distance h/b in this configuration varies from 5 to 100, whereas the Frank circuit radius is determined to be $R_c/b = 50$. A crucial point to emphasize is that the alignment of the rotation axis parallel to the disclination line results in the formation of a wedge disclination [15]. Moreover, the disclination is believed to form by means of a continuous dislocation distribution, which are depicted as kink bands. The importance of applying the idea of continuous distribution in this investigation is emphasized, as elucidated in Equation (4. 12). The magnitude of disclination rotation is expressed as [1, 15]:

$$\omega_{theory} = 2\sin^{-1}\left(\frac{b}{h}\right). \tag{4. 13}$$

Undoubtedly, the Li disclination model is unquestionably better suitable assessing misorientation angles in high-angle grain boundaries. Hence, the model devised by Gertsman is superior for smaller misorientation angles. Nevertheless, as this work is the initial endeavor to quantitatively assess the Frank vector using the holonomy approach, we have decided to use the Li model and we will compare our theoretical predictions [55]. Figure 4. 1 (b) displays the results obtained through holonomy approach and predictions given by the theory of grain boundary. The black circles depict the outcomes derived from the holonomy study, whereas the solid curve corresponds to the predictions. This comparison study indicates the holonomy approach aligns well with the predictions described in Equation (4. 13). Furthermore, there is a clear pattern in which the size of the Frank vector escalates as the proximity between dislocations diminishes. The increase in intensity is ascribed to the greater concentration of dislocations created at the kink boundary, which occurs when the proximity between dislocations diminishes. An further crucial aspect pertains to the assessment of the Frank vector when the kink band exhibits an angle ψ, as depicted in Figure 4.1(c). The presence of tilted kink interfaces is a common occurrence in kink deformations, particularly in ridge kink models. Therefore, this aspect has significant importance. The angle ψ is adjusted between -40 and 40 degrees in this specific configuration.

The Burgers vector direction aligned with the x_1 direction, while maintaining a consistent dislocation distance of $h'/b' = 5$ along the x_2 axis. Therefore, alterations in the interface angle directly affect the theoretical prediction, which is represented as a function of the interface angle, denoted as:

$$\omega'_{theory} = 2\sin^{-1}\left(\frac{b'\cos\psi}{2h'/\cos\psi}\right). \tag{4. 14}$$

The numerical analysis and theoretical predictions based on Equation (4. 14) are shown for various interface angles, ψ, in Figure 4. 1 (d). Significantly, the magnitude of the Frank vector decreases notably when the interface angle deviates from $\psi = 0$. This phenomenon arises due to the progressive change in the angle of the interface, resulting in a decrease of dislocation density in kink boundary. This reduction is attributed to the consistent spacing between dislocations in the x_2 axis, namely $h'/b' = 5$. However, the holonomy analysis constantly shows a quantitative concurrence with the predictions, even when taking into account different interface angles.

The validation procedure proceed with the Burgers vector aligned in parallel to the kink interface, as shown in Figure 4. 1(e). Similarly to the preceding scenario, the validation of the Frank vector encompasses a range of dislocation distances, specifically from 5 to 100, where h/b is the ratio of the dislocation height to the Burgers vector. Given the parallel alignment of the Burgers vector with the kink interface, it is expected that the magnitude of the Frank vector will be zero. The expectation is verified by the holonomy study depicted in Figure 4. 1(f), where a slight discrepancy is observed at $h/b = 5$. Nevertheless, as the majority of data points constantly match the theoretical prediction, this tiny divergence might be deemed insignificant. Although a significant amount of degree of freedom, exceeding 11 million, was employed, it is still considered inadequate for achieving accuracy at short dislocation distances. However, the results obtained from the holonomy analysis demonstrate a close agreement with theoretical predictions, even in cases where the Burgers vector aligns parallel to the kink interface.

In order to complete the validation procedure, we examine a dislocation configuration where the direction of the Burgers vector is always perpendicular to the kink interface. We then systematically change the angle ψ of the interface. In a manner resembling the situation depicted in Figure 4. 1(b), the interface angle covers a range of -40 to 40 degrees while keeping the dislocation distance constant at $h/b = 5$. Figure 4. 1(h) illustrates small discrepancies between the results obtained from the holonomy study and the theoretical expectations. The changes mostly occur as a result of computational inaccuracies, even though mesh refinement is implemented around the kink interface. Nevertheless, despite these minor inconsistencies, the largest variation detected is 4.6%, which confirms the ongoing accuracy of calculations using the holonomy method. Essentially, despite these little variations, the outcomes derived from the holonomy study of the four dislocation configurations confirm the efficacy of this approach in accurately quantifying the disclination Frank vector in various dislocation arrangements.

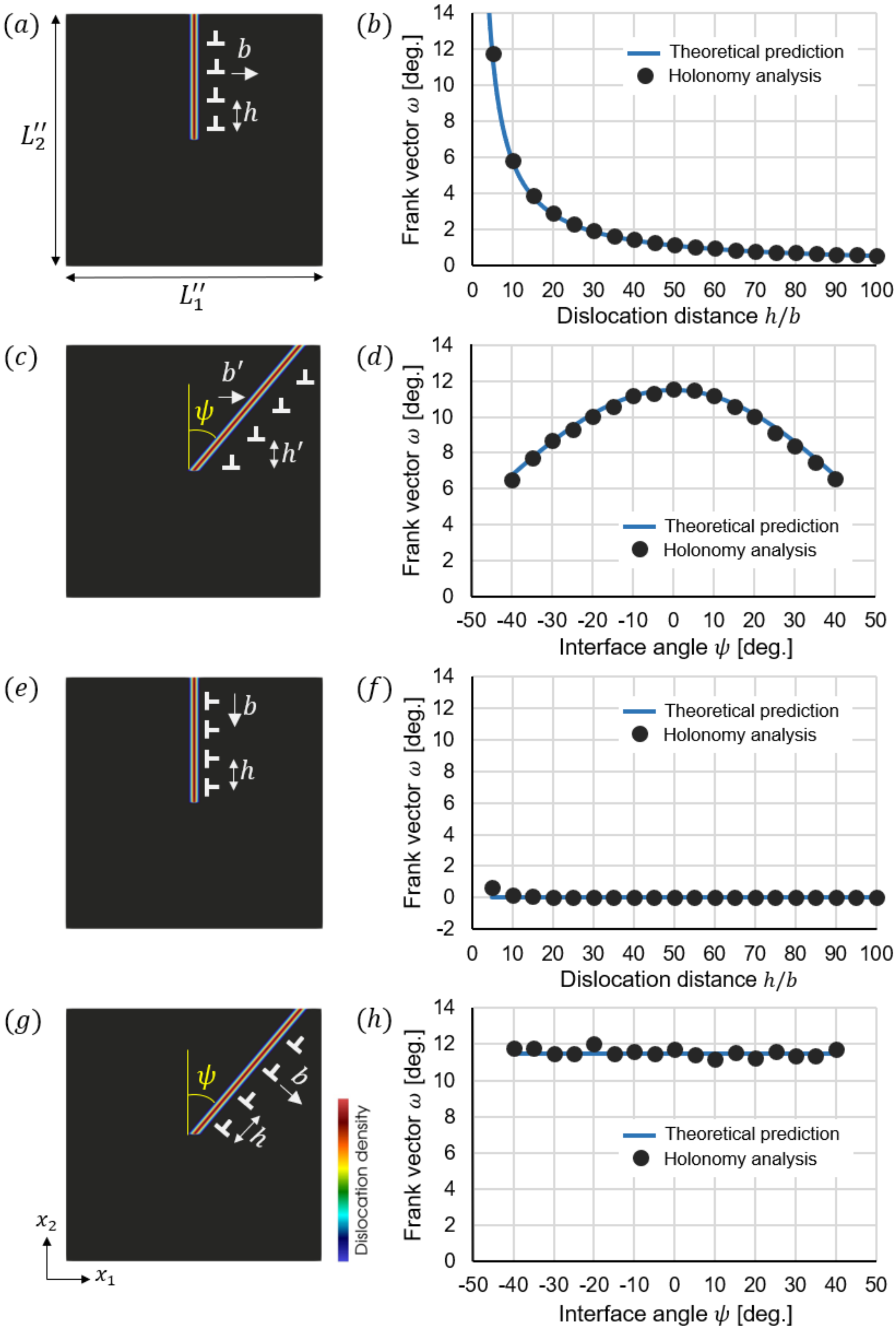

Figure 4. 1 provides a validation of holonomy method across several dislocation configurations. (a) represents the dislocation arrangement when the Burgers vector is perpendicular to the kink interface, whereas (b) displays the outcomes of the holonomy analysis. Subsequently, the results of holonomy analysis, denoted as (c) and (d), are obtained specifically when the kink

interface exhibits an angle. The conditions for obtaining (e) and (f) occur when the Burgers vector is aligned. Finally, (g) and (h) are acquired while the interface angle always changes, and the Burgers vector remains perpendicular to the kink interface.

4.4. Numerical analysis results

4.4.1. Simulation of a ridge kink deformation

The preceding section has illustrated the concurrence between the holonomy approach and the predictions [1]. This presentation showcases the effectiveness of the holonomy approach in evaluating the Frank vector in different dislocation arrangements. However, the previous validation was limited to a single kink interface. Thus, we broaden the utilisation of the holonomy method to a model of kink deformation characterised by a ridge structure. Here, we have created a kink deformation that involves three sets of edge dislocation arrays represented by the kink interface [14]. Figure 4. 2 (a) presents a summary of the ridge-type kink deformation in a two-dimensional model. The dimensions are normalised with $L_1/b = 1{,}000$ and $L_2/b = 1{,}000$. One array is linear and exclusively comprises positive edge dislocations, whereas the other two diagonal arrays consist of negative edge dislocations. In addition, given the slip plane is limited to basal slip, we orient the Burgers vector parallel to this plane, namely in the x_1 direction.

This work emphasises three crucial factors that impact the evaluation of the Frank vector magnitude: the ratio of dislocation distance to Burgers vector, the angle between interfaces, and the ratio of the radius of the Frank circuit to the Burgers vector. The dislocation distance along a linear kink interface is defined within the range of 5 to 100 times the Burgers vector length h/b, while the interface angle ranges from 10 to 40 degrees ψ, and the radius of the Frank circuit runs from 5 to 100 times the Burgers vector length R_c/b. Our assertion is based on the presence of dislocations within a single slip plane. Therefore, the dislocations on the diagonal interface are aligned in the same direction as those on the linear kink interface. Figure 4. 2(b) displays an example of the ridge-type kink model obtained from numerical analysis. It exhibits an interface angle of $\psi = 20°$ and a dislocation distance of $h/b = 5$. Nevertheless, because of the unclarity of the dislocation density distribution, we focus on examining the region around the tip of the kink interface. This precise area is where we assess the Frank vector. The enlarged area of the kink interface, indicated by a yellow dashed box in Figure 4. 2(b), is shown in Figure 4. 2(c). The dimensions of this extended region are $L_1''/b = 50$ and $L_2''/b = 50$. The figure clearly shows a uniform distribution of dislocation density along the kink contact, which is important for applying the theory of continuous dislocation density distribution described by Equation (4. 12).

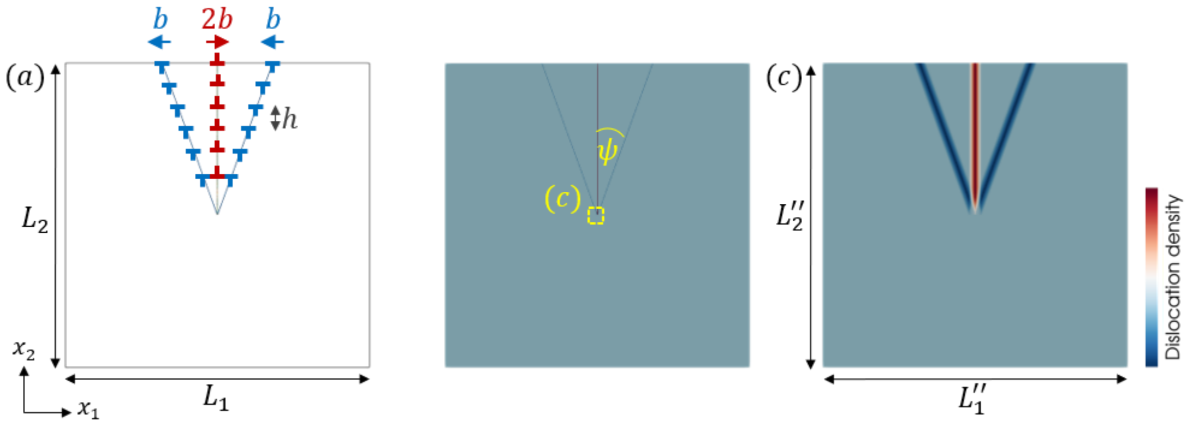

Figure 4. 2(a) depicts the ridge kink deformation model, where the dimensions are specified as $L_1/b = 1{,}000$ ans $L_2/b = 1{,}000$. (b) shows the macroscopic deformation of the ridge kink model. (c) presents the distribution of dislocation density, as marked in yellow box in (b).

4.4.2. Macroscopic deformation of the ridge kink model

The ridge-type kink deformation consists of three kink interfaces that are defined by both positive and negative planar arrays of edge dislocations. The objective of this part is to confirm if the macroscopic deformation matches the characteristic patterns reported in experimental ridge-type kink models [21]. In order to achieve this objective, we methodically manipulate the dislocation distance within the range of 5 to 100 times the ratio of the dislocation height to the Burgers vector, denoted as h/b, and the interface angle between 10 and 40 degrees, denoted as ψ. The results constantly show a clear pattern: when the dislocation distance along the kink interface decreases, there is significant macroscopic deformation. This correlation is consistent with the anticipated outcome, as shorter distances of dislocation result in a greater density of dislocations along the kink contact. This observation bears resemblance to the investigation conducted by Pranoto et al. on ortho-type kink deformation [49], suggesting that shorter distances between dislocations lead to higher bending angles. Hence, the number of dislocations generated at the kink interface has a direct impact on the magnitude of macroscopic deformation.

Figure 4. 3 illustrates the macroscopic deformation at various interface angles, while keeping the dislocation distance at a ratio of of $h/b = 5$. Significantly, there is a clearly visible protrusion on the upper surface of the model, which is a defining feature of the ridge kink model and aligns with experimental findings [21]. This notable feature manifests as an elevated

region with two contrasting subregions, mimicking a protuberant structure. The degree of this significant deformation is considerably controlled by the magnitude of the interface angle. More precisely, when ψ is equal to 10°, the intense deformation is limited to a certain region. This region then gradually expands as the contact angle increases, as depicted in Figure 4. 3(a) through (d). The macroscopic deformations produced from numerical analysis correspond qualitatively with those found in experimental research, which validates the accuracy of the model.

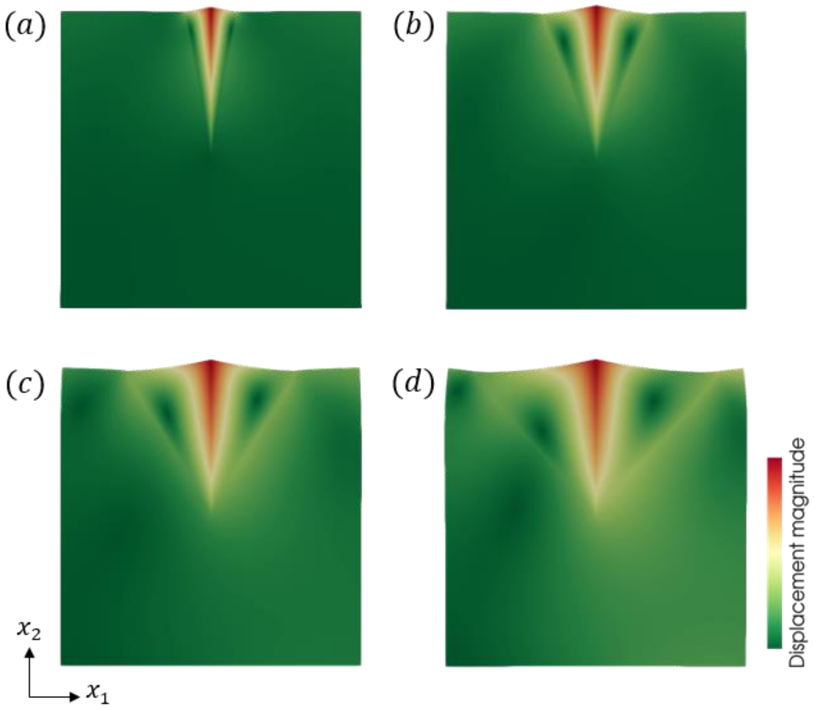

Figure 4. 3 shows the macroscopic deformation of the ridge kink model at different interface angles. More precisely: (a) $\psi = 10°$, (b) $\psi = 20°$, (c) $\psi = 30°$, and (d) $\psi = 40°$.

4.4.3. Application of the holonomy method into ridge kink deformation

The comprehensive validation conducted in the preceding section, which specifically targeted a singular kink interface, has convincingly shown that the holonomy approach fits quantitatively with the theoretical predictions put out by the grain boundary theory [1]. The consistency of these findings across different dislocation arrangements clearly suggests the dependability of the holonomy method in accurately evaluating the intensity of disclinations by measuring the Frank vector. Therefore, the purpose of this section is to expand the use of the holonomy method to the ridge kink model in order to accurately verify the presence of disclinations. The ridge-type kink model consists of three kink interfaces, as shown in Figure 4. 2(a). The theoretical expression for measuring the Frank vector is as follows:

$$\omega_{theory} = \left(2\sin^{-1}\left(\frac{b}{h}\right)\right) - \left(2 \times\ 2\sin^{-1}\left(\frac{b}{2h}\cos^2\psi\right)\right) \tag{4. 15}$$

In order to begin our investigation, we examine the Frank vector at various dislocation distances ranging from 5 to 100. We maintain a fixed radius of the Frank circuit at$R_c/b = 50$, while altering the interface angles. Figure 4. 4(a) displays the results obtained from the holonomy study in conjunction with the theoretical forecasts. The holonomy analyses are depicted using green open squares, blue open triangles, and red open circles, which correspond to interface angles of 20°, 30°, and 40°, respectively. The solid curves depict the theoretical predictions based on Equation (4. 15) for each interface angle, aligning with the color schemes of the holonomy analyses. The holonomy investigations at various interface angles show a significant correlation with the theoretical expectations. This highlights the flexibility of the holonomy analysis, expanding its usage to not only single kink interfaces but also ridge-type kink models. Significantly, there is a clear pattern that develops, indicating that the Frank vector generally increases as the distance between dislocations decreases. Furthermore, the magnitude of the Frank vector consistently grows as the interface angle increases.

We will now analyze the Frank vector in relation to the radius of the Frank circuit. We will modify the Frank circuit radii within the range of $5 \leq R_c/b \leq 100$, while also adjusting the interface angles between $20^{\circ} \leq \psi \leq 40^{\circ}$. It is crucial to mention that, for the sake of this investigation, we established the dislocation distance as $h/b = 10$. Figure 4. 4 displays the magnitude of the Frank vector determined by analyzing holonomy across four different interface angles. The data points are depicted using various forms and colors: green unfilled squares indicate 20°, blue unfilled triangles represent 30°, and red unfilled circles denote 40°. The solid curves represent the theoretical predictions for each interface angle, which are consistent with the colors assigned to the holonomy analysis. The results consistently demonstrate a uniform size of the Frank vector, irrespective of changes in the radius of the Frank circuit. In essence, the magnitude remains same regardless of variations in the radius of the Frank circuit. Moreover, the highest magnitude of the Frank vector corresponds to an interface angle of 40 degrees, which is consistent with the observations presented in Figure 4. 4(a). Although there is a little difference between the holonomy studies and the theoretical predictions, this difference is most noticeable at the 40° contact interface. However, on average, the deviation remains less than 9%. Therefore, despite these minor variations, the holonomy study shows significant quantitative agreement with the theoretical expectations.

The examination of the ridge kink model reveals several points. The holonomy approach is a reliable and effective technique for measuring the Frank vector in various dislocation configurations, including both singular and multiple kink interfaces, such as those found in the ridge-type kink deformation model. We find a considerable link between the Frank vector and both the dislocation distance and the interface angle. Significantly, we find no discernible correlation between the magnitude of the Frank vector and the radius of the Frank circuit. This indicates that the magnitude of the Frank vector remains constant regardless of variations in the radius of the Frank circuit. The presence of disclinations in kink deformations is efficiently demonstrated using Frank vector measurements achieved using the holonomy method.

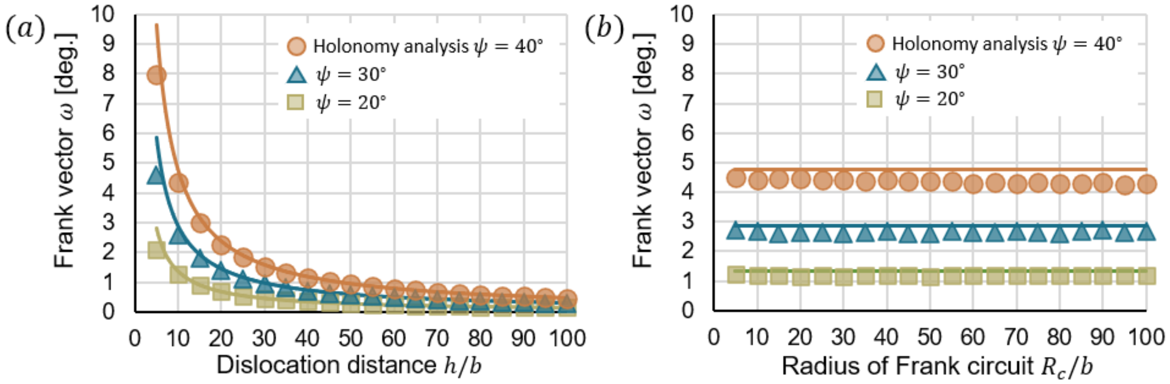

Figure 4. 4(a) shows the magnitude of the Frank vector acquired for the dislocation distance at various interface angles, whereas (b) represents the Frank vector with respect to the radius of Frank circuit

4.4.4. Analysis of stress fields caused by disclinations

The magnitude of the Frank vector is determined by two crucial parameters: the ratio of dislocation distance to Burgers vector (h/b) and the interface angle (ψ). Conversely, variations in the Frank circuit's radius R_c/b appear to have minimal effect, suggesting that changes in the circuit's size do not affect the magnitude of the Frank vector. Nevertheless, the importance of the magnitude of the Frank vector becomes evident when the distance of dislocation diminishes, and it increases significantly with greater interface angles. An important discussion emerges over the impact of the Frank vector's size on the distribution of the elastic stress field. The distribution of this stress field is mainly observed around the tip of the kinks, where disclinations are formed. However, prior research has not fully explained the finding of this elastic stress field due to multiple limitations.

Figure 5 displays the distribution of the elastic stress fields obtained from the ridge-kink model, taking into account interface angles of 10 and 40 degrees. More precisely, we have established the dislocation distance to be $h/b = 5$ along a linear kink interface. The upper figures illustrate the distribution of stress fields obtained at an interface angle of 10 degrees, while the bottom figures portrays the distribution of stress fields obtained at an interface angle of 40 degrees. Subfigures (a) and (b) depict the normal stress components, whereas subfigure (c) illustrates the shear stress component at the 10-degree interface angle. Following that, subfigures (d) and (e) provide the normal stress components, whereas subfigure (f) demonstrates the shear stress for the interface angle of 40 degrees. It should be emphasized that a stress field study was performed for interface angles of 20 and 30 degrees as well, however, these particular findings are not included in this discussion.

In order to begin our study, we investigate the distribution of stress fields that correspond to a 10-degree interface angle. The model exhibits prominent stress concentrations mostly in the upper region, while the concentration at the tip of the kink interface is rather modest. More precisely, the concentration is only present at the abrupt protrusion in the S_{11} normal stress component. In contrast, both the S_{22} normal stress and the shear stress S_{12} exhibit a high level of concentration at the higher point of the inclined kink interface, with a small dispersion observed around the ridge kink structure. Defining the stress field distribution at the kink interface tip within the material is a challenging task. The uncertainty emerges because of the short interface angle, which leads to a reduced magnitude of the Frank vector. When the interface angle is modest, the dislocations around the kink interface tip are located in close proximity. The presence of dislocations with opposite Burgers vector signs on the same slip plane results in attractive interaction, effectively canceling each other out. However, when the interface angles reach 40 degrees, the stress field exhibits a wider and more broad dispersion.

The stress field distribution at an interface angle of $\psi = 40°$ is illustrated in Figures 5(d) to (f). These figures demonstrate a far wider distribution osf the stress field. When examining the normal stress component S_{11}, it is not only present in the sharp protrusion but also extends towards the lower part near the termination of the three kink interfaces. The expansion is caused by the greater separation between dislocations near the kink interface tip, which enables each dislocation array to create its own elastic stress field. Likewise, the stress distribution found in component S_{22} is not confined around the ridge kink structure; instead, it expands outward beyond the kink interface. Furthermore, the magnitudes of all the normal stress components exceed those of the shear stress components, emphasizing the crucial role of normal stress in enhancing material strength, supporting the previous findings of Pranoto and colleagues [49].

The examination of the stress fields yields numerous significant observations. The Frank vector has a substantial impact on both the absolute values and the spatial distribution of the stress fields. When the magnitude of the Frank vector is modest, the stress concentration is minor and mostly limited to certain spots in the top area of the model. Nevertheless, when the scale of the Frank vector grows, the elastic stress fields dispersion widens. Furthermore, regardless of the angle circumstances of the kink interface, the magnitudes of the normal stress components greatly exceed those of the shear stress components. This emphasizes the increased impact of the typical stress components in controlling the strength of materials in kink deformation situations, such as LPSO-type magnesium alloys. Furthermore, the dispersion of the stress field in the S_{12} shear stress component plays a role in the interaction between disclinations and other defects, due to its wider distribution throughout the medium. The Peach-Koehler force exerted on dislocations, as described by classical dislocation theory, can be mathematically represented as $F_k = t_j \times \left(\sigma_{ij} b_j\right)$, where t_j, σ_{ij} and b_j represent the dislocation tangent direction, linearized Cauchy stress, and Burgers vector, respectively. The cross symbol $\times$ represents the outer product. Here, we assume that the elastic stress is equivalent to the linearized Cauchy stress.

The analysis of the stress fields provides several key observations. Primarily, the magnitude of the Frank vector significantly influences both the absolute values and the spatial distribution of the stress fields. There exists a direct correlation between the magnitude of the Frank vector and both the absolute values and the spatial spread of the stress field. When the Frank vector magnitude is small, the stress concentration is minimal and confined primarily to specific points in the upper region of the model. However, as the magnitude of the Frank vector increases, the distribution of the elastic stress fields expands. Additionally, across all interface angle conditions, the absolute values of the normal stress components substantially surpass those of the shear stress components. This highlights the heightened influence of the normal stress components in governing material strength in kink deformation scenarios, such as LPSO-type Mg alloys. Moreover, the stress field distribution within the shear stress component S_{12} contributes to the interaction between disclinations and other defects, owing to its broader distribution across the medium. According to classical dislocation theory, the Peach-Koehler force acting on dislocations can be expressed as $F_k = t_j \times \left(\sigma_{ij} b_j\right)$, where t_j, σ_{ij}, and b_j denote the dislocation tangent direction, linearized Cauchy stress, and Burgers vector, respectively. Here, the cross symbol × signifies the outer product. In this scenario, we assume that the second Piola-Kirchhoff stress corresponds to the linearized Cauchy stress. Hence, the Peach-Koehler force escalates in direct proportion to the linearized Cauchy stress, thereby augmenting the impediment encountered by dislocations, rendering their movement more arduous owing to the resistance exerted by the stress field.

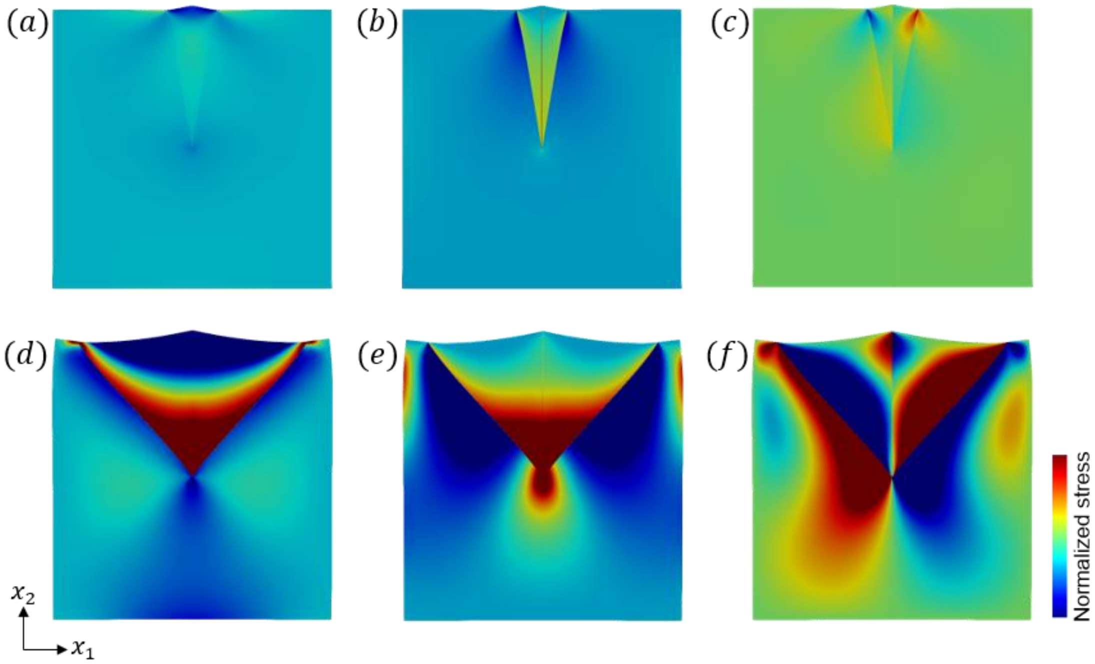

Figure 4. 5(a), (b), and (c) represent the stress field distributions obtained at an inteface angle of 10 degrees, whereas (d), (e), and (f) represent the stress distributions obtain at an interface angle of 40 degrees.

Chapter V

Modeling and Numerical Analysis of Eshelby Twist and Twist Boundary Based on Differential Geometry

5.1. Introduction

Nanomaterials, characterized by dimensions on the nanoscale, exhibit distinctive mechanical properties that differ from their bulk counterparts. The strength and malleability of metals at this size have garnered significant interest because of their potential use in ensuring the dependability and ease of production of small-scale devices [56]. It is vital to underscore that material properties within this scale range exhibit size-dependent characteristics. The surface area-to-volume ratio of nanoscale materials is substantially higher than that of larger-scale counterparts, and this factor plays a crucial role. Consequently, the increased surface area enhances interactions between nanomaterials and their surrounding environments, resulting in strengthened material properties. However, despite their excellent mechanical properties, it is noteworthy that nanomaterials can also exhibit lattice defects, such as dislocations. Therefore, understanding the behavior of dislocations in nanomaterials is crucial for effectively controlling their mechanical properties.

The formation mechanism of nanowires is typically understood to entail a vapor-liquid-solid process, in which metal particles serve as catalysts to promote nucleation and induce growth in a single direction [57]. Zhang [58] discusses another method of nanowire generation that involves an axial screw dislocation. Eshelby performed a theoretical examination of screw dislocations that were oriented in parallel with the axis of a rod during the 1950s [59]. His work demonstrated that screw dislocations generate torque in the finite medium, resulting in twisting deformation, now recognized as the Eshelby twist. Subsequently, Zhu and colleagues, using transmission electron microscopy (TEM), identified chiral branched nanowires with an axial screw dislocation at the central axis [60]. Notably, no screw dislocation was detected in the branches. This observation aligns with the studies of Bierman et al., who reported that the growth mechanism of one-dimensional nanowires is not catalyst-dependent but is instead driven by an axial screw dislocation along the length of nanowires [18]. Furthermore, twisting deformation in nanowires can also occur when two screw dislocations intersect perpendicularly, resulting in what is known as a twist boundary. However, the study on nanowires induced by twist boundaries has not received widespread attention.

The aim of this study is to demonstrate the resemblance in twist deformation caused by the Eshelby twist and twist boundary models, utilizing nonlinear continuum mechanics grounded in differential geometry.

5.2. Geometrical theory of dislocations

5.2.1. Riemann-Cartan manifold

We present a concise overview of the geometric theory of dislocations on the Riemann-Cartan manifold, as formulated by Yavari and Goriely [6], and also by Kobayashi and Tarumi [3]. In this theoretical framework, the kinematics of continuum mechanics can be described in three unique configurations: the reference $\mathcal{R}$, intermediate $\mathcal{B}$, and current $\mathcal{S}$ configurations. The interconnection of these configurations is achieved via the multiplicative decomposition of the deformation gradient. To analyze the motion of a continuous material, local coordinate systems are used for each configuration. These coordinate systems are denoted as $(dx^i) = (dx^1, dx^2, dx^3)$, $(\vartheta^i) = (\vartheta^1, \vartheta^2, \vartheta^3)$, and $(dy^i) = (dy^1, dy^2, dy^3)$. Thus, the connection between both coordinate systems is explained in the following manner:

$$\vartheta^i = (F_p)^i_j dx^j, \quad dy^i = (F_e)^i_j \vartheta^j, \quad dy^i = F^i_j dx^j = (F_e)^i_j (F_p)^k_j dx^j. \tag{5. 1}$$

From now on, we will use the summation convention for indices that are repeated. Likewise, we can express the Riemannian metrics g_R,g_B and g_S for the reference, intermediate, and current configurations using the deformation gradients.

$$\begin{gathered} g_{\mathcal{R}} = \delta_{ij} dx^i \otimes dx^j, \quad g_{\mathcal{B}} = \delta_{ij} (F_p)^i_k (F_p)^j_l dx^k \otimes dx^l, \\ g_{\mathcal{S}} = \delta_{ij} (F_e)^i_k (F_e)^j_l \vartheta^k \otimes \vartheta^l. \end{gathered} \tag{5. 2}$$

In these formulas, δ_{ij} represents the Kronecker delta, and $\otimes$ signifies the tensor product. By applying the principles of elastoplasticity theory, the elastic strain may be obtained by analyzing the Green strain tensor E. The amount of the elastic strain is established by comparing the Riemannian metrics in the current and intermediate configurations. The Green strain tensor can be represented using the following expression:

$$E = \frac{1}{2}(g_{\mathcal{S}} - g_{\mathcal{B}}) = \frac{\delta_{ij}}{2}\left(F^i_k F^j_l - (F_p)^i_k (F_p)^j_l\right) dx^k \otimes dx^l. \tag{5. 3}$$

Furthermore, the elastic deformation is determined by include the intermediate configuration $\mathcal{B}$ within the conventional three-dimensional Euclidean space. More precisely, this mapping process produces the current configuration by reducing the elastic strain energy.

5.2.2. The dislocation density tensor and Cartan first structure equation

To simulate dislocations in nanowires, we utilise the notion of continuous distribution, which is represented by the dislocation density tensor [22]. The dislocation density tensor consists of two components: the Burgers vector, represented as $b^i\ \partial/\ (\partial x^i)$, and the tangential vector along the dislocation line, defined as $n^j \delta_{jk} dx^k$. The dislocation density tensor is defined as follows:

$$\alpha = f b^i n^j \delta_{jk}\, dx^k \otimes \frac{\partial}{\partial x^i}. \tag{5. 4}$$

The symbol "f" represents the continuous distribution function that defines the dislocation density. As per Kondo's hypothesis [7], the dislocation density tensor and the torsion 2-form are aligned within the context of differential geometry. Hence, the utilisation of differential geometry is crucial when applying the theory of continuous dislocation distribution. The connection between the dislocation density tensor and the torsion 2-form is formed by applying the Hodge star operator, as defined in Equation (5. *5*)

$$\tau =* \alpha = \sum_{j<k} f b^i n^j \epsilon_{jkl} dx^k \wedge dx^j \otimes \frac{\partial}{\partial x^i}, \tag{5. 5}$$

The symbol ϵ_{jkl} denotes the permutation tensor. Moreover, there is a link between the torsion 2-form τ and the plastic deformation gradient F_p, as evidenced by the following equation.

$$\tau^i = \frac{\partial \left(F_p\right)^i_j}{\partial x^k}\, dx^k \wedge dx^j. \tag{5. 6}$$

By substituting ϑ^i with $\left(F_p\right)^i_j dx^j$ in Equation (5. *1*) and incorporating it into Equation (5. *6*), we derive the ensuing expression

$$\tau^i = d\vartheta^i. \tag{5. 7}$$

This expression is recognized as the Cartan first structure equation.

5.2.3. Stress equilibrium equation and elasticity equatioon

Let's begin by examining a continuous mapping, represented as y, that describes the transformation of the intermediate configuration $\mathcal{B}$ within the Riemann-Cartan manifold into the current configuration $\mathcal{S}$ in Euclidean space. The present configuration $\mathcal{S}$ is derived by reducing the elastic strain energy using the St. Venant-Kirchhoff hyperelastic model, as mentioned previously. To be more precise, the strain energy functional is formulated in the following manner.

$$W = \int_{\mathcal{R}} \frac{1}{2} C_{ijkl} E_{ij} E_{kl} \det F_p dV. \qquad (5.\ 8)$$

The elastic coefficients in this expression are represented by the symbol C_{ijkl}. To simplify the analysis, we assume elastic isotropy by introducing a normalized shear modulus $G = 1$ and a Poisson ratio $G = 1$. In accordance with the variational principle, the attainment of the stationary state for the strain energy functional, $\delta W = 0$, results in the elastic deformation of hyperelastic material. Here, we propose the introduction of a test function $\left(h^i\right) = (h^1, h^2, h^3)$ that satisfies the constraint $h^i = 0$ at the Dirichlet boundary. Therefore, the condition of being stationary can be expressed in the following manner

$$\int_{\mathcal{R}} C_{ijkl} \delta_{mn} \frac{\partial h^m}{\partial x^i} \frac{\partial y^n}{\partial x^j} E_{kl} \det F_p = 0. \qquad (5.\ 9)$$

This equation depicts the state of stress equilibrium in a weak form.

5.2.4. Isogeometric analysis

This section addresses the two equations: the plasticity and the elasticity equations numerically through isogeometric analysis (IGA). IGA is a variant of the Galerkin method that employs non-uniform rational B-spline (NURBS) basis functions. NURBS basis functions are utilized in IGA to concurrently represent the geometric shape and perform numerical analysis of the domain [61]. The Cox-de Boor recursion formula provides a way to express B-spline basis functions.

$$B^i_{(J^i,p^i)}\left(t^i\right) = \frac{\xi^i - \xi^i_{Ji}}{\xi^i_{p^i+J^i} - \xi^i_{J^i}} B^i_{(J^i,p^i-1)}\left(t^i\right) + \frac{\xi^i_{J^i+p^i+1} - \xi^i}{\xi^i_{p^i+J^i+1} - \xi^i_{J^i+1}} B^i_{(J^i+1,p^i-1)}\left(t^i\right), \qquad (5.\ 10)$$

J^i represents the element number, p^i denotes the polynomial degree of B-spline basis functions, and ξ^i refers to the knot vector. The zero th-order B-spline function, denoted as $B^i_{(J^i,0)}\left(t^i\right)$, is equal to 1 if $\xi^i_{J^i} \leq \xi^i < \xi^i_{J^i+1}$. Otherwise, $B^i_{(J^i,0)}\left(t^i\right)$. The NURBS basis function is defined by utilizing the B-spline basis function in a manner that

$$N^I(t) = B^1_{(J^1,p^1)}(t^1)\, B^2_{(J^2,p^2)}(t^2)\, B^3_{(J^3,p^3)}(t^3). \qquad (5.\ 11)$$

Here, $t = (t^1, t^2, t^3)$ is set on the left side, and subscripts (J^1, J^2, J^3) on the right side are collectively represented by subscript I. Let n be the number of all NURBS basis functions constructed in this way, then the coordinates $\left(x^i\right)$ of each point in the reference configuration

$\mathcal{R}$, the unknown function (y^i) and the test function (h^i) are given by coefficients (x_I^i), (y_I^i) and (h_I^i) can be expressed as follows.

$$x^i(t) = \sum_{I=1}^{n} x_I^i N^I(t), \quad y^i(t) = \sum_{I=1}^{n} y_I^i N^I(t), \quad h^i(t) = \sum_{I=1}^{n} h_I^i N^I(t). \tag{5. 12}$$

Obviously, the coefficient x_I^i can be determined from the reference configuration $\mathcal{R}$ of the continuum to be analyzed. The coefficients y_I^i and h_I^i are taken such that $y^i = 0$ and $h^i = 0$ at the Dirichlet boundary Γ_D. By substituting Equation (5. 11) into (5. 7), we obtain a nonlinear equation simultaneously with the remaining coefficient y_I^i as unknown.

5.2.5. Dislocation-based modeling for nanowires

The current investigation involves the construction of nanowire models with two unique dislocation configurations. Figure 5. 1(a) and (b) depict visual illustrations of the Eshelby twist and twist boundary models, respectively. The Eshelby twist model is constructed by placing a single screw dislocation at the center of the model. Conversely, the twist boundary model is formed by the intersection of two screw dislocations, subsequently distributed along the longitudinal direction of the nanowire, as shown in Figure 5. 1(b). Moreover, it is important to emphasize that the dimensions of these models are normalized by the magnitude of the Burgers vector, denoted as b. Here, both L_1 and L_2 share equal lengths within the range of $10 \leq L_1/b \leq 10^6$. Moreover, the length of L_3 is tenfold greater than that of L_1.

In order to represent the screw dislocations in both configurations, we utilize the theory of continuous dislocation density distribution. In this context, the variable f represents a function that describes the dislocation density, while the variable r represents the distance from the center of the dislocation core. The continuous distribution of dislocation density is expressed as follows.

$$f(r) = \begin{cases} \frac{3}{\pi R^2}\left(1 - \frac{r}{R}\right) & r \leq R \\ 0 & r > R \end{cases}. \tag{5. 13}$$

Here, $3/\pi R^2$ is the normalized coefficient and R denotes the radius of dislocation core.

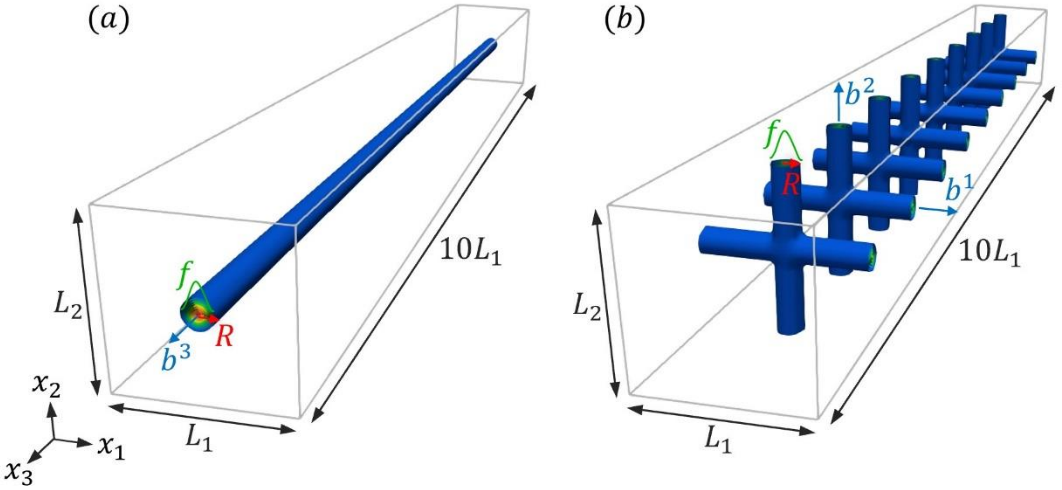

Figure 5. 1 (a) illustrates the dislocation configuration for the Eshelby model, whereas (b) shows the dislocation configuration for the twist boundary model.

5.3. Numerical analysis results

5.3.1 The influence of material size on deformation

The nanowire model consists of two distinct dislocation configurations, as depicted in Figure 5. 1. These configurations consist of a single screw dislocation for the Eshelby twist model and arrays of screw dislocations for the twist boundary model. Additionally, the Eshelby twist model is labeled as Model I, while the twist boundary model is reffered to as Model II. Importantly, the model dimensions are adjustable to investigate the size dependence of the nanowires. Thus, we vary L_1 within the range of $10 \leq L_1/b \leq 1{,}000$, and L_3 set at 10 times the length of L_1.

Figure 5. 2 illustrates the macroscopic deformation obtained from both models. Figures (a) to (d) show the macroscopic outcomes from the Eshelby twist model, while Figures (e) to (h) depict the macroscopic deformation from the twist boundary model. From the resulting macroscopic deformation, several following points can be drawn as follows. First, the twisting deformations observed in Model I (see figures (a) to (d)) agree with the experimental results conducted by Eshelby. Notably, the twisting deformation maintains uniformity along the longitudinal direction of the nanowire, validating the accuracy of the model derived through numerical analysis. The second noteworthy point pertains to the twisting deformation generated by Model II. Although the similarities exist between the twisting deformation produced by Model I and II, a fundamental difference lies in the twist distribution. In Model II, the twisting deformation is non-uniform; specifically, it is localized around the dislocation.

This observation is attributed to the distribution of dislocation density within the dislocation core.

These results imply that the twisting deformation in nanowires is not solely attributed to a single screw dislocation but instead emerges from arrays of screw dislocations, as illustrated in the twist boundary model. However, to induce twisting deformation in Model II requires the Burgers vector to maintain the same sign. Differing signs of the Burgers vector within the twist boundary model do not result in twisting deformation. This is closely related to the distribution of plastic deformation field, which will be discussed in more detail in the next section. Additionally, we note that the degree of twisting deformation is prominent in smaller dimensions. However, as the material dimensions increase, the degree of twisting deformation gradually decreases. This observation underscores the size-dependence of the material. This suggests that twisting deformation is limited to small-scale materials and is not observed on a larger scale, even though dislocations are present at larger scales.

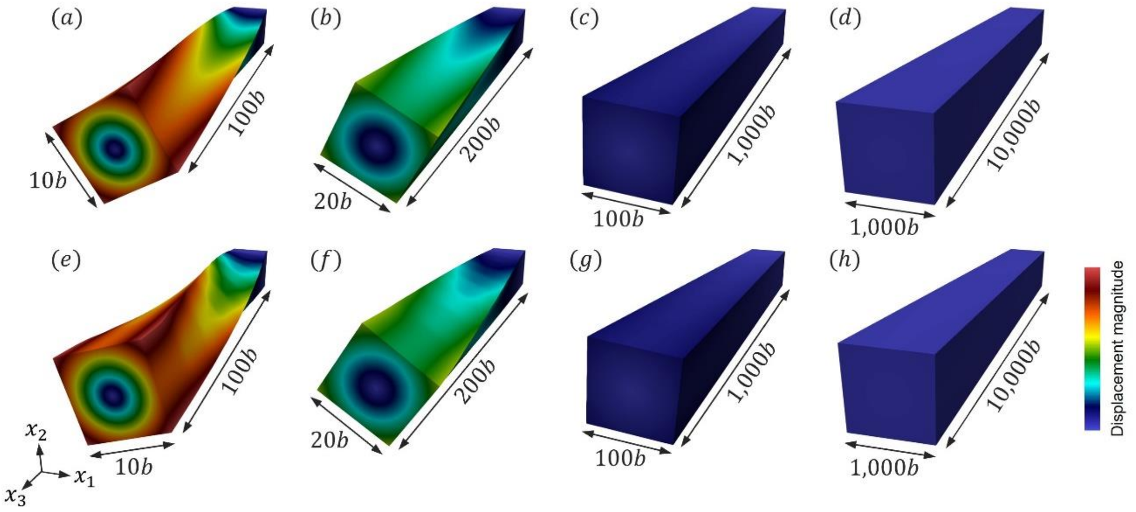

Figure 5. 2 shows the macroscopic deformation derived from the Eshelby twist and twist boundary models. The twisting deformation in the two models exhibits similarity, despite the differences in dislocation configurations. (a) through (d) represent the twisting deformation demonstrated by the Eshelby twist model, whereas (e) through (h) illustrate the twisting deformation obtained by the twist boundary model.

5.3.2 Strain energy for the Eshelby twist and twist boundary models

In the previous section, we have discussed how twisting deformation in nanowires becomes more pronounced as they decrease in size. However, the underlying mechanisms of twisting deformation increased significantly at smaller dimensions remains insufficiently elucidated. Therefore, this section aims to clarify the reasons for the increasing significance of twisting deformation by examining strain energy across different dimensions. Figure 5. 3 shows the twist angle and strain energy obtained at various model dimensions.

Figure 5. 3 (a) distinctly demonstrates that the twist angle exhibits significant prominence at smaller dimensions. More precisely, as the dimensions of the model increase, the twist angle gradually decreases, highlighting the manifestation of the size effect. For a deeper insight into twisting deformation, we further investigated by quantifying strain energy in both models. Consequently, Figure 5. 3(b) illustrates the magnitude of the strain energy across several model dimensions. Evidently, the strain energy exhibits a monotonic decreases as the model dimensions increase. Thus, this observation helps to clarify why the magnitude of the twist angle diminishes notably at larger dimensions.

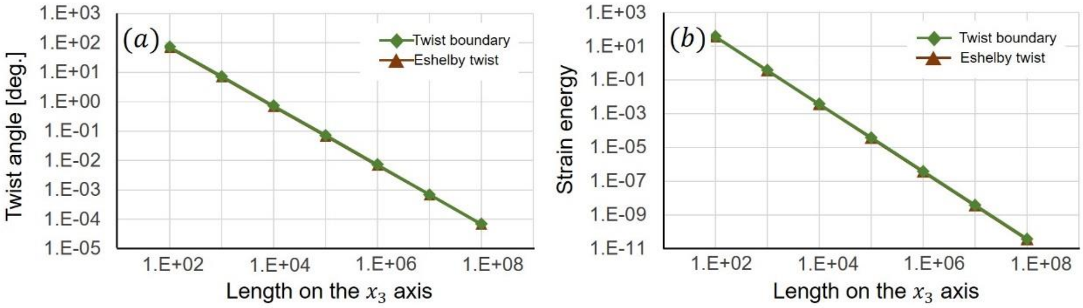

Figure 5. 3(a) represents the twist angle obtained by the Eshelby and twist boundary models, while (b) corresponds to the strain energy. Here, both the twist angle and strain energy decrease as the model dimensions increase.

5.3.3 The distribution of plastic deformation fields

As the Eshelby twist and twist boundary models manifest similar twisting deformation despite significant differences in their dislocation configurations, it is apparent that the twisting deformation from the Eshelby twist model demonstrates uniformity along the longitudinal axis of the nanowires. Conversely, the twist deformation induced by the twist boundary model appears non-uniform, primarily localized around the twist boundary. Hence, the objective of this section is to examine the similarity in twisting deformations induced by both models through the distribution of the plastic deformation field, which is derived from the Cartan first structure equation.

Figure 5. 4 showcases the plastic deformation field distribution obtained from the Eshelby twist model. According to the Cartan first structure equation, we obtain the plastic deformation gradient for three components: ${F_p}_1^3$, ${F_p}_2^3$, and ${F_p}_3^3$. However, only the ${F_p}_1^3$ and ${F_p}_2^3$

components are visualized, as the ${F_p}_3^3$ component exhibits comparatively lower values. Specifically, Figure 5. 4(a) portrays the distribution of the ${F_p}_1^3$ component in the reference configuration, while Figure 5. 4(b) illustrates the plastic deformation field distribution in the current configuration. Similarly, Figure 5. 4(c) and (d) depict the distribution of plastic deformation field in the reference and current configurations for the ${F_p}_2^3$, respectively. In the reference configuration, it is observed that the plastic deformation field distribution concentrates around the dislocation core. However, the plastic distribution field not only concentrates at the dislocation core but also extends outward, reaching the surface due to the influence of the free surface. Moving on to the current configuration, we observe that the plastic deformation field rotates counterr clockwise around the x_3 axis. Consequently, the Eshelby twist model induces twisting deformation, which has been confirmed through experimental study.

Remarkably, although both the Eshelby twist and twist boundary models demonstrate similar twisting deformations, there exists a contrast in the distribution of the plastic deformation field, even though both demonstrating rotation about the x_3 axis. Figure 5. 5 portrays the plastic deformation field obtained from the twist boundary model. In contrast to the distribution in the Eshelby twist model, the twist boundary model showcases four distinct components: ${F_p}_2^1$, ${F_p}_3^1$, and ${F_p}_1^2$. Figure 5. 5(a) illustrates the ${F_p}_1^2$ component in the reference configuration, while Figure 5. *5*(b) depicts it in the current configuration. Notably, the plastic deformation field in the current configuration also induces a counterclockwise twist along the x_3 axis. This twisting phenomenon is also evident in the other three components displayed in Figure 5. 5(d), (f), and (h). Consequently, the plastic deformation field observed in the twist boundary model results in a twisting deformation to that of the Eshelby twist model.

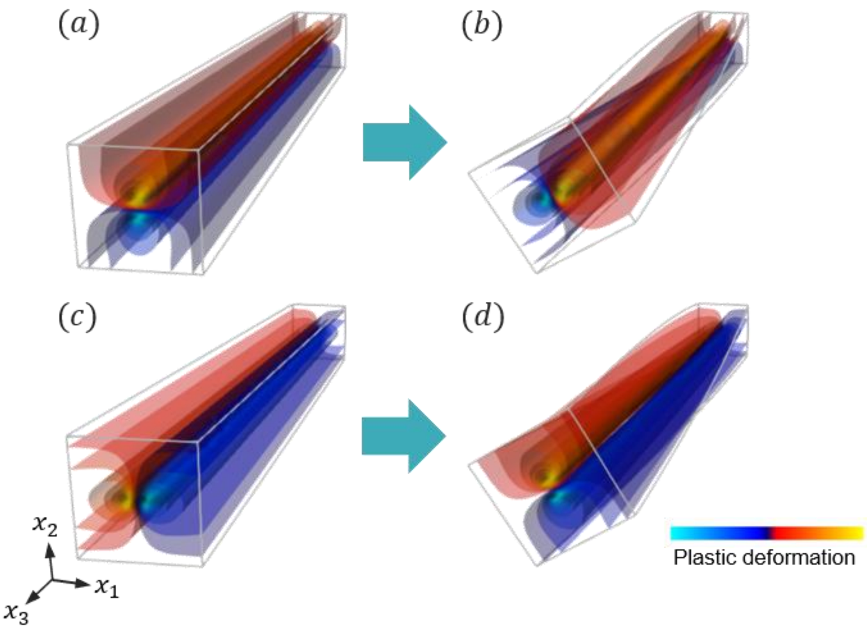

Figure 5. 4 presents the distribution of the plastic deformation fields obtained from the Eshelby twist model. (a) represents the ${F_p}_1^3$ component acquired in the reference configuration, while (b) represents it in the current configuration. (c) and (d) show the ${F_p}_2^3$ components acquired in the reference and current configurations, respectively.

There exist fundamental distinctions between the Eshelby twist model and the twist boundary model. For instance, in the Eshelby twist model, if the sign of the Burgers vector is reversed from positive to negative, a twisting deformation still emerges but in the opposite twisting deformation. This contrasts with the mechanism of twist deformation in the twist boundary model. To induce twist deformation in the twist boundary model, it is essential for the sign of the Burgers vector to remain consistent. For instance, Figure 5. 5 is generated using a Burgers vector with a positive sign. When the sign of the Burgers vector differs, twisting deformations do not manifest in the twist boundary model, as the plastic deformation fields counteract each other, preventing the formation of twist. These findings further confirm that the twisting deformation in nanowires, typically attributed to the presence of screw dislocations, as explained by the Eshelby twist model, can similarly arise through the twist boundary model with the same sign of the Burgers vector.

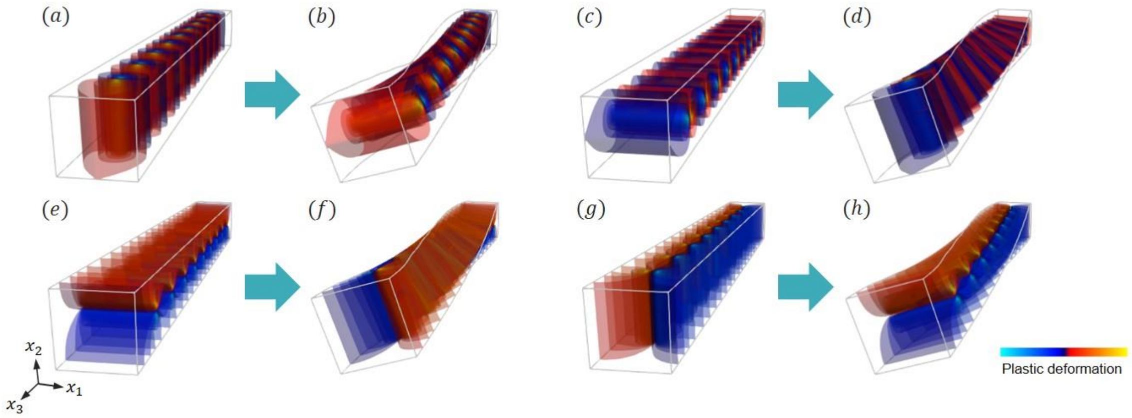

Figure 5. 5 exhibits the distribution of plastic deformation field obtained by the twist boundary model. (a) shows the distribution of the plastic deformation field on the ${F_p}_1^2$ component in the reference configuration, while (b) illustrates it in the current configuration. Similarly, (c) and (d) show the ${F_p}_2^1$ components, (e) and (f) illustrate the ${F_p}_3^1$ components, and (g) and (h) depict the ${F_p}_3^2$ components.

Chapter VI

General Conclusion

6.1 Ortho-type kink deformation

The current study involved the utilization of dislocation-based modeling and numerical analysis to examine kink deformation microstructure. Special focus was given to the energy and kinematics of the disclination that formed at the tip of the kink interface. The conclusion can be succinctly stated as:

(1) The ortho-type kink deformation model is formulated by utilizing planar arrays of edge dislocations. The dislocation density is constructed using a level-set function, and numerical analysis is performed on the Cartan first structural equation and stress equilibrium equation using the finite element method. The numerical simulation has almost 8 million degrees of freedom.

(2) The current numerical analysis provides evidence that our model accurately replicates the pronounced bending deformations at the kink interface, which aligns with the appearance of the ortho-type kink deformation reported in experimental studies. The bending angle θ has been quantitatively verified by comparing it with the prediction provided by grain boundary theory. With the exception of small calculation mistakes caused by the absence of finite element meshes, there is a satisfactory confirmation of agreement for the analysis of kink deformation.

(3) The strain energies are assessed for the growth process of the two kink models. The findings indicate that the energy exhibits symmetry in relation to the interface length H, resulting in the highest value when the kink interface tip is positioned at the middle of the model, namely when $H/L_3 = 0.5$. Additionally, we discovered that the magnitude of the strain energy may be ascribed to both the self-energy and elastic interaction energy of the disclinations.

(4) The stress field study showed that the magnitude of the normal stress components is approximately ten times higher than the shear stresses. Therefore, the normal stresses contribute to the self-energy of the disclinations. Nevertheless, due to the concentration of normal stress components in the vicinity of disclination cores, it is improbable for long-range elastic interactions to take place. In order to have a successful interaction, the distance should be no greater than 1,000b.

(5) Applying an external force is necessary to surpass the barrier of strain energy and enable plastic deformation to occur via kink deformation. Therefore, the energy directly influences the magnitude of deformation in materials susceptible to kinking. Nevertheless, the energy is greatly influenced by the development process, making it impossible to deduce the plastic deformation resistance just from the kink microstructure acquired post-deformation.

6.2 Ridge-type kink deformation

We utilized the holonomy method, which draws upon ideas from differential geometry, as a means of identifying disclinations in kink deformations. We conducted a thorough examination with meticulous validations and analysis of both a single kink interface with various dislocation configurations and the more intricate ridge-type kink deformation model. The following is a concise summary of our main findings and conclusions:

(a) The holonomy method was thoroughly validated on a single kink interface, which included a wide range of dislocation configurations. The results demonstrated a robust concurrence between the holonomy method and the theoretical forecasts generated from the grain boundary theory. This validation highlights the precision of the method in measuring the Frank vector across a wide range of dislocation configurations. The holonomy method was applied to the ridge-type kink deformation model, resulting in a quantitative agreement with the theoretical predictions of the grain boundary theory. Thus, this method effectively verified the existence of disclinations in kink deformations.

(b) The development of the ridge kink model entailed the utilization of the level-set function to depict three planar arrays of edge dislocations. The magnitude of the Frank vector is intricately linked to both the magnitude and spatial arrangement of the stress field. When the magnitude of the Frank vector is modest, the level of stress concentration is minimal, mostly concentrated at specific spots in the upper region of the model. On the other hand, when the Frank vector magnitude grows, the elastic stress field dispersion widens. Furthermore, irrespective of the interface angle, the magnitudes of the normal stress components continuously surpass those of the shear stress components.

(c) The holonomy method was implemented to the ridge kink deformation model, showing a quantitative agreement with the theoretical predictions derived from the grain boundary theory. This application success validated the existence of disclinations in kink deformations, hence demonstrating the trustworthiness of the approach.

(d) The magnitude of the Frank vector is primarily influenced by two key factors: the ratio of dislocation distance to Burgers vector (h/b) and the angle of the interface (ψ), as indicated by numerical analyses. Conversely, variations in the radius of the Frank circuit R_c/b had a comparatively minor impact on the magnitude of the Frank vector.

6.3 Eshelby twist and twist boundary

The current study involved dislocation-based modeling and numerical analysis of the Eshelby and twist boundary models, resulting in the following conclusions:

(a) The magnitude of twist angles is notably significant at small scales in both the Eshelby twist and twist border instances, showing the manifestation of size dependence.

(b) The Eshelby twist is characterized by the influence of two plastic deformation components on the twisting deformation, whereas the twist boundary is influenced by four plastic deformation components. More precisely, the Eshelby model is controlled by the ${F_p}^{3}_{1}$ and ${F_p}^{3}_{2}$ components, whereas in the twist boundary model, it is influenced by components ${F_p}^{1}_{2}$, ${F_p}^{1}_{3}$, ${F_p}^{2}_{1}$ and ${F_p}^{2}_{3}$.

(c) For the twist boundary model, only Burgers vectors that have the same sign are capable of inducing the twisting deformation.

(d) We have effectively proven that the introduction of twist deformation in nanowires may be achieved not only through the utilization of the Eshelby twist model, but also by employing the twist boundary model.

List of Publications

[Papers]

1. Sigiet Haryo Pranoto, Shogo Yokota, Shunsuke Kobayashi, and Ryuichi Tarumi. Mechanics and Energetics of Kink Deformation Studied by Nonlinear Continuum Mechanics Based on Differential Geometry. Materials Transactions, Vol. 64, No. 9 (2023) pp. 2261 to 2269.
2. Sigiet Haryo Pranoto, Shogo Yokota, Daiki Oka, Shunsuke Kobayashi, and Ryuichi Tarumi. Evaluation of Disclination Frank Vector in Ridge Kink Microstructure. Philosophical Magazine, Part A: Materials Science.

[Conferences]

1. Sigiet Haryo Pranoto, Shunsuke Kobayashi, and Ryuichi Tarumi. Modeling and Numerical Analysis of Screw Dislocations in Nano-Scale Materials. Bioengineering Colloquium 2022 (Poster presentation). Osaka University, July 22, 2022.
2. Sigiet Haryo Pranoto, Shunsuke Kobayashi, and Ryuichi Tarumi. Modeling and Numerical Analysis of Screw Dislocations Based on Differential Geometry. 15th World Congress on Computational Mechanics & 8th Asian Pacific Congress on Computational Mechanics (Oral Presentation). Yokohama (Online), July 31 – August 5, 2022.
3. Sigiet Haryo Pranoto, Shunsuke Kobayashi, and Ryuichi Tarumi. Effect of Twist Boundary on Deformation of Nanocrystalline Materials. The 35th Computational Mechanics Conference of the Japan Society of Mechanical Engineers (Poster Presentation), November 16-18, 2022.
4. Sigiet Haryo Pranoto, Shunsuke Kobayashi, and Ryuichi Tarumi. Modeling and Numerical Analysis of Screw Dislocations in Nanowires Based on Continuum Mechanics. The 6th International Conference on Materials and Reliability (Oral Presentation), Yamaguchi University, December 7-9, 2022.
5. Sigiet Haryo Pranoto, Shogo Yokota, Daiki Oka, Shunsuke Kobayashi, and Ryuichi Tarumi. Modeling and Numerical Analysis of Kink Deformation Based on Geometrical Elasto-Plasticity Theory. The 5th International Symposium on Long-Period Stacking/Order Structure and Mille-feuille Structure (Oral Presentation), Prince Hotel Shinagawa, December 11-14, 2022.

6. Sigiet Haryo Pranoto, Shunsuke Kobayashi, and Ryuichi Tarumi. Modeling and Numerical Analysis of Kink Deformation Based on Differential Geometry. BioColloquium 2023. Osaka University, July 6th 2023.

References

[1] D. Hull and D.J. Bacon, Introduction to dislocations Fourth Edition, Butterworth-Heinemann. (2001).

[2] V. Volterra: Anna. Scient. De I'Ecole. Norm. Super. **24** (1907) 401-517.

[3] S. Kobayashi and R. Tarumi: ArXiv:2205.02443v2.

[4] R. Peierls, The size of a dislocation, *Proceedings of the Physical Society,* **52** (1940), pp. 34-37.

[5] M. Lazar, Non-singular dislocation continuum theories: strain gradient elasticity vs Peierls-Nabarro model, *Philosophical Magazine,* **97** (2017).

[6] A. Yavari and A. Goriely: Arch. Ratio. Mech. Ana. **205** (2012) 59-118.

[7] K. Kondo, RAAG. **1** (1955) 6-17.

[8] B. A. Bilby, R. Bullough and E. Smith: Proceed. Royal. Soc. London. **231** (1955) 263-273.

[9] E. Kröner and A. Seeger: Arch. Ratio. Mech. Ana. **3** (1959) 97-119.

[10] A. Inoue, Y. Kawamura, M. Matsushita, K. Hayashi and J. Koike: J. Mater. Res. **16** (2001) 1894-1900.

[11] Y. Kawamura, K. Hayashi, A. Inoue and T. Matsumoto, *Rapidly solidified powder metallurgy* $Mg_{97}Zn_1Y_2$ *alloys with excellent tensile yield strength above 600 MPa.* Materials Transactions 42(7) (2001), pp. 1172-1176.

[12] T. Itoi, T. Seimiya, Y. Kawamura and M. Hirohashi: Scripta. Mater. **51** (2004) 107-111.

[13] E. Orowan: Nature **149** (1942) 643-644.

[14] J.B. Hess and C.S. Barret: Metals Trans. **185** (1949) 599-606.

[15] J. C. M. Li, Disclination model of high angle grain boundaries, *Surface science,* **31** (1972), pp. 12-26.

[16] T. Inamura: Acta Mater. **173** (2019) 270-280.

[17] Q. Wu, Q. Miao, Y. Zhang, H. Gao, and D. Hui, Mechanical properties of nanomaterials: A review, *Nanotechnol,* **9** (2020), pp. 259-273.

[18] M. J. Bierman, Y. K. A. Lau, A. V. Kvit, A. L. Schmitt, S. Jin, Dislocation-driven nanowire growth and Eshelby twist, *Science*, **320** (2008), pp. 1060-1063.

[19] D.C. Jillson: Trans. Metall. AIME **188** (1950) 1009-1018.

[20] J.J. Gilman: J.O.M. **6** (1954) 621-629.

[21] T. Tokuzumi, M. Mitsuhara, S. Yamasaki, T. Inamura, T. Fuji and H. Nakashima: Acta Materialia. **248** (2023) 118785.

[22] J. F. Nye, Some geometrical relations in dislocated crystals, *Acta metallurgica,* **1** (1953), pp. 153-159.

[23] S. Kobayashi and R. Tarumi: Trans. JSME. **87** (2021) 894 [in Japanese].

[24] V. V. Kaminskii, E. Abe, Y. Kawamura, L. M. Dorogin, A. E. Romanov, *Kinking in LPSO Mg-Zn-Y alloys and other layered materials.* Reviews on Advanced Materials and Technologies **4**(2) (2022), pp. 15-31.

[25] L. Benabou, *Finite strain analysis of wood species under compressive failure due to kinking.* International Journal of Solids and Structures 49(3-4) (2012), pp. 408-419.

[26] M. S. Paterson, L. E. Weiss, *Experimental folding in rocks.* Nature 195(4846) (1962), pp. 1046-1048.

[27] J. Kim, S. Sandlobes, D. Raabe, *On the room temperature deformation mechanisms of a Mg-Y-Zn alloy with long-period-stacking ordered structures.* Acta Materialia 82 (2015), pp. 414-423.

[28] M. W. Barsoum, L. Farber, T. El-Raghy, *Dislocations, kink bands, and room-temperature plasticity of* Ti_3SiC_2. Metallurgical and Materials Transactions A, 30(7) (1999), pp. 1727-1738.

[29] T. Schaden, F. D. Fischer, H. Clemens, *Numerical modelling of kinking in lamellar γ-TiAl based alloys.* Advanced Engineering Materials, 8(7) (2006), pp. 1109-1113.

[30] T. Nizolek, N. A. Mara, I. J. Beyerlein, J. T. Avallone, T. M. Pollock, *Enhanced plasticity via kinking in cubic metallic nanolaminates.* Advanced Engineering Materials, 17(6) (2014), pp. 781-785.

[31] R. Racek, N. A. Mara, I. J. Beyerlein, J. T. Avallone, T. M. Pollock, *Enhanced plasticity via kinking in cubic metallic nanolaminates.* Advanced Engineering Materials, 17(6) (2014), pp. 781-785.

[32] Z. Liu, Q. Zheng, J. Z. Liu, *Stripe kink microstructures formed in mechanical peeling of highly oriented pyrolytic graphite.* Applied Physics Letters, 96(20) (2010), pp. 201909.

[33] M. A. Wadee, G. Hunt, M. Peletier, *Kink band instability in layered structures.* Journal of the Mechanics and Physics of Solids, 52(5) (2004), pp. 1071-1091.

[34] M. Yamasaki, K. Nyu, and Y. Kawamura, *Corrosion behavior of rapidly solidified Mg-Zn-Y alloy ribbons.* Materials Science Forum 419-422(2) (2003), pp. 937-942.

[35] M. Yamasaki, M. Matsushita, K. Hagihara, H. Izuno, E. Abe, Y. Kawamura, *Highly ordered 10-type long-period stacking order phase in a Mg-Zn-Y ternary alloy.* Scripta Materialia 78-79 (2014), pp. 13-16.

[36] M. Yamasaki, T. Anan, S. Yoshimoto, Y. Kawamura, *Mechanical properties of warm-extruded Mg-Zn-Gd alloy with coherent 14H long periodic stacking ordered structure precipitate.* Scripta Materialia 53 (2005), pp. 799-803.

[37] E. Abe, Y. Kawamura, K. Hayashi, A. Inoue, *Long-period ordered structure in a high-strength nanocrystalline Mg-1 at% Zn-2 at% Y alloy studied by atomic-resolution Z-contrast STEM.* Acta Materialia 50(15) (2002), pp. 3845-3857.

[38] D. H. Ping, K. Hono, Y. Kawamura, A. Inoue, *Local chemistry of a nanocrystalline high-strength Mg 97 Y 2 Zn 1 alloy.* Philosophical Magazine Letters 82(10) (2002), pp. 543-551.

[39] S. Yoshimoto, M. Yamasaki, and Y. Kawamura, *Microstructure and mechanical properties of extruded Mg-Zn-Y alloys with 14H long period ordered structure.* Materials Transactions 47(4) (2006), pp. 959-965.

[40] K. Hagihara, Z. Li, M. Yamasaki, Y. Kawamura, T. Nakano, Strengthening mechanism acting in extruded Mg-based long-period stacking ordered (LPSO) phase alloys, *Acta Materialia,* **163** (2019), pp. 226-239.

[41] K. Hagihara, Z. Li, M. Yamasaki, Y. Kawamura, T. Nakano, *Strengthening mechanism acting in extruded Mg-based long-period stacking ordered (LPSO)-phase alloys.* Acta Materialia 163 (2019), pp. 226-239.

[42] K. Hagihara, M. Yamasaki, Y. Kawamura, T. Nakano, *Strengthening of Mg-based long-period stacking ordered (LPSO) phase with deformation kink bands.* Materials Science & Engineering A 763 (2019) 138163.

[43] K. Hagihara, N. Yokotani and Y. Umakoshi: Intermetallics 18 (2010) 267-276.

[44] K. Hagihara, T. Tokunaga, K. Nishiura, S. Uemichi, S. Ohsawa, *Control of kink-band formation in mille-feuille structured Al/Al_2Cu eutectic alloys.* Materials Science & Engineering A 825 (2021) 141849.

[45] F. R. N. Nabarro, *Physics of strength and plasticity.* Cambridge, MA: The MIT Press (1969), pp. 97.

[46] A. E. Romanov and V. I. Vladimirov: Phys. Stat. Sol. **78** (1983) 11-34.

[47] A. E. Romanov and V.I. Vladimirov. In: F.R.N. Nabarro, editor, Amsterdam: North-Holland. 1992. P. 191.

[48] R. De Wit: continual theory of disclinations. Moskow: Mir; 1977 [in Russian].

[49] S. H. Pranoto, S. Yokota, S. Kobayashi, and R. Tarumi, *Mechanics and energetics of kink deformation studied by nonlinear continuum mechanics based on differential geometry.* Materials Transactions 64(9) (2023).

[50] A. A. Nazarov and A. E. Romanov, *On the average misorientation of general tilt boundaries.* Philosophical Magazine Letters 60 (1989), pp. 187-193.

[51] M. Murayama, J. M. Howe, H. Hidaka, and S. Takaki, *Atomic-level observation of disclination dipoles in mechanically milled*, nanocrystalline Fe. Science 295 (2002), pp. 2433-2435.

[52] M. O. Katanaev, *Geometric theory of defects.* UFN 175 (2005), pp. 705-733 (in Russian).

[53] S. Kobayashi and R. Tarumi: Trans. JSME. **87** (2021) 896 [in Japanese].

[54] L. W. Tu, *Differential geometry.* Springer International Publishing (2017), pp.112-113.

[55] V. Yu. Gertsman, A. A. Nazarov, A. E. Romanov, R. Z. Valiev, and V. I. Vladimirov, *Disclination-structural unit model of grain boundaries.* Philosophical Magazine A 59 (1989), pp. 1113-1118.

[56] C. R. Weinberger and W. Cai, Orientation-dependent plasticity in metal nanowires under torsion: twist boundary formation and Eshelby twist.

[57] R. S. Wagner, W. C. Ellis, Vapour-liquid-solid mechanism of single crystal growth.

[58] H. F. Zhang, C. M. Wang, L. S. Wang, Helical crystalline SiC/SiO2 core-shell nanowires.

[59] J. D. Eshelby, Screw dislocations in thin rods, *Journal of Applied Physics,* **24** (1953), pp. 176-179.

[60] J. Zhu, H. Peng, A. F. Marshall, D. M. Barnett, W. D. Nix, Y. Cui, Formation of chiral branched nanowires by the Eshelby twist, *Nature,* **3** (2008), pp. 477-481.

[61] T. Hughes, J. Cotrrell, and Y. Bazilevs, Isogeometric analysis: CAD, finite elements, NURBS, exact geometry and mesh refinement, *Computer Methods in Applied Mechanics and Engineering,* **194** (2005), pp. 4135-4195.

Acknowledgements

I wish to convey my profound appreciation to my supervisor, Prof. Ryuichi Tarumi, whose mentorship, forbearance, and steadfast backing have been indispensable during this research journey. The insightful feedback, encouragement, and dedication of this individual have played a crucial role in shaping this dissertation. Furthermore, I would like to convey my appreciation to Prof. Shigenobu Ogata and Prof. Atsutomo Nakamura, who fulfilled the role of examiners for my thesis.

I am grateful to Kobayashi-kun for his insightful ideas, which significantly improved the quality of my work. I am profoundly grateful for his assistance, both in the research activity and in our personal lives beyond the confines of the school, since it has greatly benefitted me. Furthermore, I would want to extend my gratitude to the dislocation team, specifically Daiki Oka and Shogo Yokota, for their invaluable assistance in this work. I would also like to express my gratitude to old friends such as Hattori Karin, Naoki Inoue, Oono, Matsura, Yamamoto, and other more whom I am regrettably unable to specifically acknowledge. I would want to express my gratitude to the current members of my laboratory.

Furthermore, I would want to express my sincere appreciation to my family, namely my parents, Suwanto and Nuraini Zubaidah, for their unwavering support and devout supplications. I am profoundly grateful to my beloved spouse, Nurul Azizah, whose steadfast support and encouragement played a crucial role in my academic journey. I would want to extend my apologies to my son, Evano Althaf Pranoto, for my absence in the three years following his birth. I am appreciative of the unwavering support and motivation provided by my elder sister, Lia Apriyanti, and younger brother, Fandy Novianto Herlambang, who continually uplifted my spirits.

The author sincerely acknowledges the financial assistance provided for this work by the Japanese Government (MEXT/Monbukagakusho) Scholarship and the Japan International Cooperation Agency (JICA). Additionally, the author wishes to convey his appreciation to acquaintances from the Osaka-Nara Indonesian Student Association (PPI) and the Osaka Muslim Association (OMA) at Osaka University.